Pontificia Universidad
JAVERIANA
Cali

Facultad de Ingeniería
y Ciencias

Acta de Correcciones al Proyecto de Grado
Ingeniería Electrónica

Fecha: Septiembre 7 del 2021

Autores: Isabella López Cifuentes

Nombre del Proyecto de Grado: IN-SILICO DESIGN OF AN ALL-ARMCHAIR GRAPHENE NANORIBBON FIELD EFFECT TRANSISTOR SENSOR FOR THE INDIRECT DETECTION OF STARCH

Director: Andrés Jaramillo Botero, PhD

Como indica el artículo 2.27 de las Directrices de Trabajo de Grado, he verificado que los estudiantes indicados arriba han implementado todas las correcciones que los Jurados del Proyecto de Grado definieron que se efectuaran, como consta en el Acta de Calificación correspondiente.

Firma de Director(a) del Proyecto de Grado
Andres Jaramillo Botero

Nota de Aceptación

Aprobado por el Comité de Trabajo de Grado en cumplimiento de los requisitos exigidos por la Pontificia Universidad Javeriana para optar el título de Ingeniera Electrónica.

Camilo Rocha

HERNÁN CAMILO ROCHA NIÑO, PhD
Decano de la Facultad de Ingeniería

LUIS EDUARDO TOBÓN LLANO, PhD
Director Carrera Ingeniería Electrónica.

ANDRÉS JARAMILLO BOTERO, PhD
Director(a) Trabajo

LUIS EDUARDO TOBÓN LLANO, PhD
Jurado 1

Juan Manuel Marmolejo Tejada.

JUAN MANUEL MARMOLEJO TEJADA, PhD
Jurado 2

In-silico design of an all-armchair graphene nanoribbon field effect transistor (GNRFET) sensor for the indirect detection of starch

Isabella López Cifuentes

Thesis

Advisor
Andrés Jaramillo Botero, PhD.

Pontificia Universidad Javeriana Cali
Facultad de Ingeniería y Ciencias
Departamento de Electrónica y Ciencias de la Computación

Santiago de Cali, September 2021

Acknowledgements

This work was partially funded by the "OMICAS program: Optimización Multiescala Insilico de Cultivos Agrícolas Sostenibles (Infraestructura y validación en Arroz y Caña de Azúcar)" Scientific Ecosystem belonging to the Colombia Científica Program, sponsored by The World Bank, The Ministry of Science, Technology and Innovation (MINCIENCIAS), ICETEX, the Colombian Ministry of Education and the Colombian Ministry of Commerce, Industry and Turism, under GRANT ID: FP44842-217-2018, OMICAS Award ID: 792-61187.

First and foremost, to my advisor Andres Jaramillo-Botero for his guidance, knowledge, patience, and support in the completion of this document. Thanks to Gustavo Lara for optimizing and providing me with the REAXFF file used in this work.

To mom and dad for their unconditional support and patience during my undergraduate studies, to my brothers for providing me with distractions and funny memes during lockdown. To Daniel, for being there for me and pushing me to never give up. To my friends, for their sympathetic ear, for their motivation, and for making every day in and outside the office always fun.

To the universe.

Abstract Starch plays a fundamental role in plants, being an essential molecule to understand their energy transport and storage. Therefore, continuous monitoring of the intracellular synthesis of starch is critical for understanding energy pathways and metabolic regulation in plants. This work highlights the importance of real-time measurement of ultra-low concentration of this metabolite, to detect and manage stress-induced events in plants. Thus, we present the in-silico design of an all-armchair graphene nanoribbon field-effect transistor (GNRFET) device for the detection of ultra-low concentration (pM-nM) amylose. Starch molecules are composed primarily of two glucose polymers: amylopectin and amylose, the latter presenting a linear structure desired for its simplicity and smaller size. We use a self-assembled monolayer (SAM) of a pyrene moiety, 3-[4-(pyren-1-yl)butanamido]phenylboronic acid (PBPBA) adsorbed on the channel, to functionalize the graphene surface. Then covalent binding of the target molecule to the end with phenylboronic acid provides mechanical, chemical, and electronic signal sensing stability. Furthermore, we screened GNRFET configurations with different widths, to control bandgap in the channel, lengths to ensure tunneling transport across the semiconducting junction, and a back-gated channel to optimize electronic transport and switching properties of the device. We demonstrate the channel SAM of PBPBA functionalization improves the signal-to-noise-ratio (SNR) of the device, and estimate its limit of detection (LOD) to be $7.123/n \times 10^{-2} mol/L$ (for a symmetric 2D array configuration with n as the number of sensor units per array dimension). The devices offers an output current sensitivity of $100 - 300nA$, at low gate voltages ($V_G = 1.2V$) and drain-to-source voltage $V_{DS} = 0.6V - 0.8V$, for the detection of 1-2 amylose trimers. Therefore we obtained a low-power all-armchair GNR-FET sensor with SAM PBPBA ligands in the channel that provides a real-time and high throughput solution for sensing amylose (a component of starch).

Resumen El almidón juega un papel fundamental al ser una molécula esencial para comprender el transporte y almacenamiento de energía en plantas. En este artículo se destaca la importancia de la medición en tiempo real de la concentración ultra baja de este metabolito, para detectar y manejar los factores externos de estrés en plantas. Por lo tanto, presentamos el diseño in-silico de un dispositivo basado en un transistor de efecto de campo conformado por nano cintas de grafeno tipo armchair para la detección de concentraciones ultra bajas (pM-nM) de amilosa. Las moléculas de almidón están compuestas principalmente por dos polímeros de glucosa: amilopectina y amilosa, en donde la última presenta una estructura lineal, deseada por su simplicidad y menor tamaño. Usamos una monocapa auto ensamblada de una molécula tipo pireno, como lo es el ácido 3-[4- (pireno-1-il) butanamido] fenilborónico o PBPBA, el cual se adsorbe físicamente sobre el canal semiconductor funcionalizando o la superficie del grafeno por medio de la estructura aromática del pireno. Adicionalmente, la interacción covalente de la molécula analito al extremo con ácido fenilborónico facilita la señal de detección al brindar estabilidad mecánica, química y electrónica del analito de interés. Además, examinamos configuraciones del sensor con diferentes anchos, para controlar la banda prohibida en el canal, diferentes longitudes para asegurar el transporte por tunelamiento cuántico a través de la unión semiconductora y usamos un canal de compuerta trasera para optimizar el transporte electrónico y las propiedades de conmutación del dispositivo. Demostramos que la capa auto ensamblada de PBPBAs sobre el canal mejora la relación señal /ruido (SNR) del dispositivo, y estimamos un límite de detección (LOD) de $7,123/n \times 10^{-2} mol/L$ (para una configuración de una matriz 2D simétrica, con el número de unidades de sensor por dimensión de matriz). Los dispositivos ofrecen una sensibilidad de corriente de salida entre 100-300nA, a voltajes de compuerta bajos ($VG = 1.2V$) y voltaje de drenaje a fuente $VDS = 0.6V - 0.8V$, para la detección de 1-2 moléculas de trímeros de amilosa. Por lo tanto, obtuvimos un sensor GNRFET de bajo consumo de energía con ligandos PBPBA funcionalizando el canal, el cual proporciona una solución en tiempo real y de alto rendimiento para detectar amilosa (un componente del almidón).

Contents

List of Tables

List of Figures

Abbreviations

GNR	**G**raphene **N**ano **R**ibbon
acGNR	arm chair **G**raphene **N**ano **R**ibbon
zGNR	zigzag **G**raphene **N**ano **R**ibbon
FET	**F**ield **E**ffect **T**ransistor
MOSFET	**M**etal **O**xide **S**emiconductor **F**ield **E**ffect **T**ransistor
GNRFET	**G**raphene **N**ano **R**ibbon **F**ield **E**ffect **T**ransistor
FED	**F**ield **E**ffect **D**evice
HOMO	**H**ighest **O**ccupied **M**olecular **O**rbital
LUMO	**L**owest **U**nnoccupied **M**olecular **O**rbital
PBPBA	**P**iren-1-yl **B**utanamido **P**henyl **B**oronic **A**cid
SAM	**S**elf **A**ssembly **M**onolayer
PBA	**P**yrene **B**uronic **A**cid
DFT	**D**ensity **F**unctional **T**heory
DFTB	**D**ensity **F**unctional **T**ight **B**inding
QM	**Q**uantum **M**echanics
BO	**B**orn -**O**ppenheimer approximation
NEGF	**N**on-**E**quilibrium **G**reen's **F**unction
MM	**M**olecular **M**echanics
MD	**M**olecular **D**ynamics
RMS	**R**oot **M**ean **S**quare
LOD	**L**imit of **D**etection

Chapter 1

Introduction

The world's increasing population, decreasing land availability due to increasing urbanization, competition for biofuel feedstocks, increasing fuel and fertilizer costs, and the uncertainty that brings climate change pose major challenges for global food production. The need for new high-yielding crop genotypes adapted to the climate and environmental changes is indispensable. Conventional breeding is no longer a solution to increase production yields, but alternative techniques relying on gene technology provide an alternative to resolve the current crisis[13].

Despite the advent of fast genome sequencing technologies at cheaper prices, genomic information alone will not solve the short-term need for increased crop yields. The use of phenomics, which aims to measure traits of organisms at different ontogenetic levels and under different environments, is required. The latter has been an alternative option to breeders to satisfy the growing demand of high-yielding and stable varieties[14].

Accurate and remote sensing is a critical component of precise phenotyping. Conventional tests involve sample taking to subject that sample to a chemical process in a laboratory or if remote, they use temporary labels (such as fluorescence, chemiluminescence, colors, etc) and specific chemical processes. For instance, conventional tests to detect metabolites such as starch comprise iodine tests [15] that use a blue-colored result after a chemical reaction between a part of the starch molecule with iodine molecules; other method consists of solubilizing starch converting it quantitatively to glucose and assaying the glucose enzymatically [16].

However, all these methods are invasive to the plant, they do not necessarily allow to perform sensing on-site or remotely and in some cases are not accurate enough, at least at a molecular level. To this end, remote in-vivo and portable ex-vivo sensing of ultra-low concentrations (pM-nM) of significant molecular substances (RNA, DNA, proteins, primary and secondary metabolites, etc) are required. Biomarker sensors offer a potential cost-effective contribution to solve this problem.

This thesis aims to optimize the design of, and characterize, a sensing device that comprises a field-effect transistor, using a single-atom-thick graphene nanoribbon semiconducting channel functionalized, to detect amylose as indirect detection of starch in plants.

1.1 Problem Statement

Sucrose and starch are primary metabolites in plants that play a fundamental role in their growth and development. Starch specifically is synthesized during the day by plants and algae to store energy in a dense inert form; when photosynthesis cannot meet the demand for energy and carbon skeletons for biosynthesis, the plant uses its starch storage to sustain metabolism and energy production. Besides, non-photosynthetic tissues, such as seeds, stems, roots, or tubers, store starch for long-term usage [17].

Sucrose and starch are essential molecules for understanding energy transport and storage in plants[14]. Therefore, continuous monitoring of their intra-cellular synthesis is critical for understanding energy pathways and metabolic regulation in plants. Changes in their levels, corresponding to the ultimate biological response to genetic differences or stresses (such as disease or environmental changes). Thus, real-time measurement of these metabolites, capable of relaying the state of these variables without compromising the health of the living organism, such as in-vivo sensing techniques, would be required. Highly efficient and reliable devices able to detect ultra-low concentration of target molecules within cells of a living organism [18].

To this end, we propose a label-free[1] Graphene Nanoribbon Field Effect Transistor (GNRFET) with a functionalized channel surface for indirect detection of starch.

---

[1] Detection method which makes use of the intrinsic properties of the target molecule (charge, molecular weight, refractive index, etc) to track it and its activity. No use of temporary labels such as fluorescence, chemiluminescence, etc are needed to detect it

Along with the development of this project we approach the following questions:

- What would be the best self-assembled chemical monolayer, capable of binding to graphene on one end and with affinity to starch on the other, without compromising detection accuracy?
- How does the analyte affect the electronic transport properties of the GNRFET sensor with a functionalized surface?
- How to optimize the electronic transport properties, based on the geometric and material characteristics of the nanosensor for the detection of starch?

Chapter 2

Objectives

2.1 General objective

- To perform in-silico[1] characterization of a graphene nanoribbon field effect transistor (gnrFET) nanosensor architecture for the selective detection of starch.

2.2 Specific objectives

1. To design and evaluate the basic FET geometric structure for the nanosensor.
2. To determine and validate an appropriate chemical group to functionalize the semiconducting channel of the nanosensor for the indirect detection of starch.
3. To characterize the electronic transport properties with/out target molecules bound to the functional group.
4. To evaluate the thermodynamic stability of the sensor under physiological temperature conditions.

---

[1] Performed via computer simulations

Chapter 3

Background theory

In this chapter, we introduce the theoretical framework essential to understanding the design and processes carried out during this project.

3.1 Plant metabolites

Metabolism comprises all chemical reactions within a living plant cell. Plant metabolites are the byproducts during metabolism and are categorized as primary or secondary. Primary metabolites comprise compounds as simple sugars, alcohols, amino-acids, etc within a plant cell and are directly involved in essential functions to the plant to survive (such as growth, development, and reproduction); secondary metabolites are not directly involved in those essential functions but play a key role in the plant's interaction with its environment. In this project, we are interested in starch as the primary metabolite as a major biological integrator of plant growth and main energy support during nocturnal activity.

3.1.1 Starch

Starch plays a fundamental role in plants. It is an essential molecule to understand energy transport and storage in plants, where it is categorized as transitory or as storage starch; the former is used to supply energy to the plant and sustain metabolism during the night, and the latter is stored for long periods to later being relocated during germination, sprouting, and regrowth of the plant. This storage starch is the one found in seeds, roots, or stems and corresponds to the starch we consume in our food and the one that describes its nutritional properties. Understanding starch biosynthesis, its composition, structure, and functionality are of enormous interest being of most importance for the targeted improvement of starch crops [17].

Because of the complexity of starch granules, and that their composition and size vary depending on the plant, we evaluated simpler and smaller molecules that we could use instead to indirectly detect starch. To this end, we considered molecules related to its biosynthesis in plants or that directly conform its structure, including ADP-glucose, amylose, and amylopectin.

3.1.1.1 ADP-Glucose

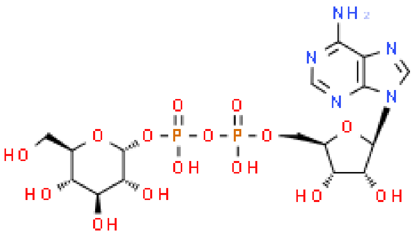

Figure 3.1: Molecular structure of ADP-Glucose. Image is taken from ChemSpider

Adenine Phosphate Glucose or ADP-glucose is the precursor and substrate molecule in the synthesis of starch in plants. ADP-glucose serves as a building block for the biosynthesis of the glucan chain. As Figure 3.2a shows, the synthesis path from sucrose obtained from photosynthesis to hexose phosphates after being metabolized in the endosperm. The hexose phosphate is combined with adenosine triphosphate (ATP) to synthesize ADP-glucose. And thereafter, starch synthases or SSs catalyze the transfer of glucosyl moiety of ADP-glucose to create α-1,4-linked chains of distinct lengths to finally synthesizing amylose and amylopectin, which together conform starch [2]. Therefore, detecting ADP-glucose could allow the detection of starch, before its synthesis in the plant.

3.1.1.2 Amylose and Amylopectin

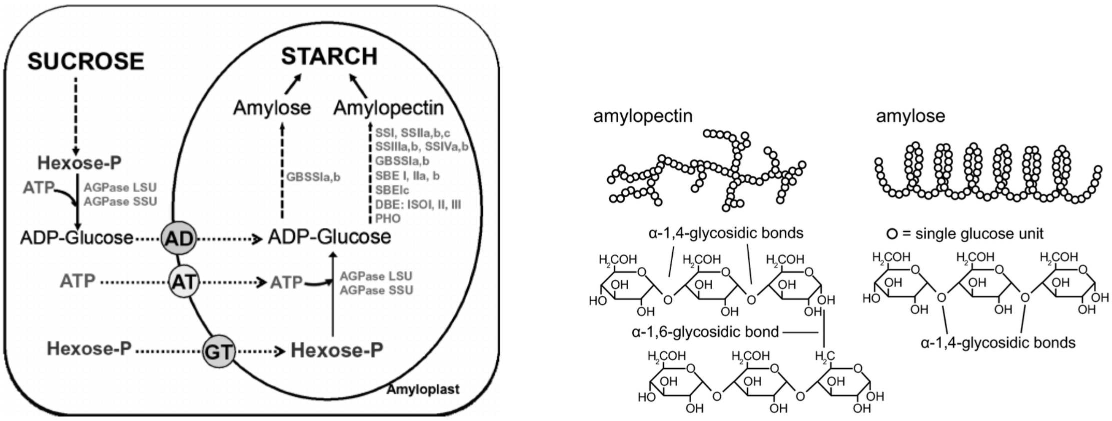

(A) (B)

Figure 3.2: Starch biosynthesis pathway (taken from [2]) (b) Molecular architecture of starch granules, conformed by amylose (top-right) which is primarily linear and have few branches, while amylopectin (top-left) is highly branched.

Structurally, starch granules consist of two glucose chains joined by α-1-4 glycosidic bonds are composed of two glucose polymers: amylopectin and amylose (Figure 3.2). Amylopectin (shown top-left in Figure 3.2) is a highly branched glucose polymer and makes around 65 to 90 % of starch granules, while amylose is considerably smaller and lightly branched. The amylose to amylopectin ratio is commonly used to describe various features of cereals (i.e. viscosity, digestability, gelatinization, etc). A wide variety of industrial uses and applications come from obtaining high or low amylose content in starches, as it affects starch digestibility and nutritional properties of the foods we eat [19].

Amylose presents an almost linear glucose polysaccharide form, which makes it a simpler molecule. The highly branched form like the one in amylopectin could present complications as a target molecule, not only for its size but steric effects within the molecule would make it difficult for a ligand to react properly and dock to the amylopectin to immobilize it. Therefore, we reduced the chance to have to deal with this issue by choosing amylose as the target molecule, also by indirectly reducing size we reduce the computational resources we would need to use it. For the same purpose, we used during this project a three $\alpha(1 \rightarrow 4)$-linked glucose-monomer (trimer amylose) as the specific target molecule.

3.2 Devices and materials

In this section, we explain the basic concepts behind inorganic material (such as Silicon, Germanium, etc) structural/compositional properties and how they relate to that of novel organic materials (i.e. graphene-based materials) used in electronic devices. Also, we describe how these properties contribute to electronic transport, hence electronic device design, and performance.

3.2.1 Solid-state materials

Isolated atoms are brought together to form a solid. Several types of interactions occur among atoms in a solid, including i) pairwise electrostatics, ii) Van der Waals interactions, and iii) 2, 3, and 4 valence type interactions. In the process, important changes may come about in the electron level configurations which result in varied electrical properties that describe each type of solid.

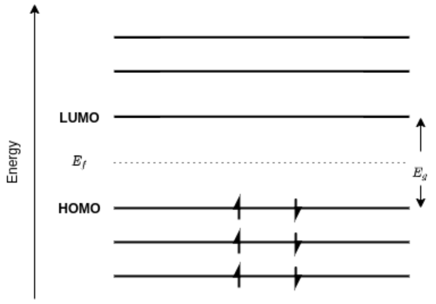

FIGURE 3.3: Molecular energy level diagram, with E_f as the Fermi energy and E_g as the energy band gap

For an isolated atom, electrons have discrete energy levels corresponding to the atomic orbitals that they occupy. Atoms essentially interact with one another through their last orbitals or the *frontier orbitals* (Figure 3.3), where we find the Highest Occupied Molecular Orbital (HOMO) and the Lowest Unoccupied Molecular Orbital (LUMO).

When a solid is formed and atoms are brought closer, as spacing becomes smaller the atomic orbitals overlap forming molecular orbitals and there must be at most one electron with a different spin per level (Pauli's exclusion principle). Then as more atoms are brought together, molecular orbitals and their corresponding energy levels become close enough to one another that they could be described as bands of energy.

When the spacing between atoms approaches its equilibrium, two bands separated by an energy gap E_g appear. In organic semiconductor literature the upper band could be referred to as the "LUMO band" and the lower band "HOMO band", and both containing allowed energy levels. On the contrary, the *energy gap*, *bandgap*, or *forbidden band* E_g contains no allowed energy levels for electrons to occupy [3, 20]. In inorganic materials and semiconductors literature (e.g., Si, GaAs, etc) the analog to these bands are the *valence* and *conducting bands* respectively[21]. Following, the definition of different types of materials is explained in terms of this nomenclature.

3.2.1.1 Conductors, insulators, and semiconductor materials

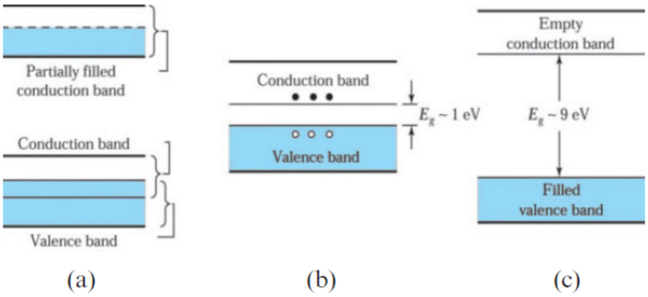

FIGURE 3.4: Energy band representations of (a) a conductor with two possibilities (partially filled conduction band shown at the upper portion of the overlapping bands shown at the lower portion), (b) a semiconductor, and (c) an insulator. Image is taken from [3]

The electrical characteristics in a solid-state crystal essentially depend on variations on its band structure as is shown in Figure3.4. There are three different types of materials based on the main features of their band structure, as defined in inorganic semiconductor nomenclature:

- **Metals or conductors:** Among their main characteristics are their low value of resistivity and a conduction band that is partially filled or overlaps the valence band (in this case there is no bandgap). Subsequently, electrons are free to move very easily when they gain kinetic energy through a small applied electric field, and as a result, a current flow might occur [3, 22].

- **Insulators:** These materials present a large bandgap, electrons occupy all energy levels in the valence band leaving the levels in the conduction band empty. Energy from an applied electric field or thermal energy would not be enough for conduction. Therefore, this material presents high resistivity; it can not conduct current [3].
- **Semiconductors:** They are, by definition, poor conductors at low temperatures, with all electrons in the valance band at $T = 0K$ but at room temperature their valence band is semi-populated and the conduction band semi-depopulated. To increase their conductivity, the electrons need to get excited thermally and obtain enough energy to jump to the conduction band. As a result, a small applied potential can easily result in a moderate current [3].

Although transport is different between inorganic and organic materials; in organic materials we also need to take into account their band structure to establish a metallic, semiconductor, or insulating-like behavior in order to design novel electronic devices. For this application, we use graphene and other organic molecules (ligands) present in the channel for the detection of the target molecule.

3.2.2 Field Effect Transistor (FET)

The Field Effect Transistor in principle is a device that controls a conductivity channel using an electric field. FET technology offers a wide range of variations, the MOSFET (Metal Oxide Semiconductor Field Effect Transistor) is one of them having three terminals: source, drain, and gate. The basic working principle consists of controlling the flow of the majority of carriers (electrons or holes) from the source to drain by affecting the dimensions and shape of a *conductive channel*, which is modified by an applied voltage across the gate/source terminals [22].

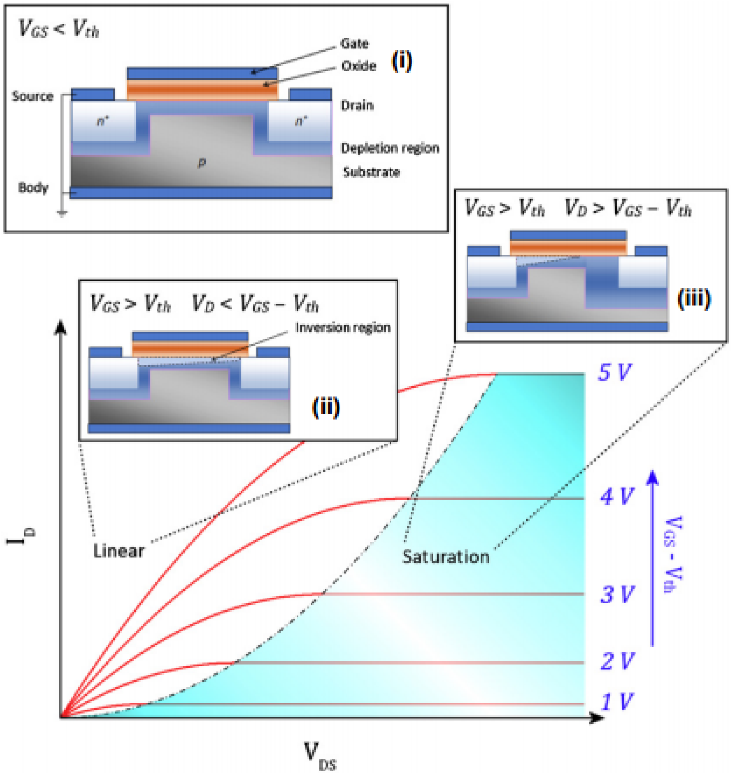

FIGURE 3.5: Relationships between the drain current, I_D, and the source-drain voltage, V_{DS}, and the relative strength of the gate voltage, V_{GS}, to the threshold voltage, V_{th}, of the device. The inserts (i–iii) show the three principal operating modes of an n-channel MOSFET, shown in cross-section, with (i) the subthreshold mode, (ii) linear mode and (iii) saturation mode. Image is taken from [4]

3.2.2.1 Metal Oxide Semiconductor Field Effect Transistor (MOSFET)

The operation of this transistor follows the basic working principle explained before, and it has three main operational modes which are illustrated in figure 3.5 [4, 22]:

- **Subthreshold mode:** (With $V_{GS} < V_{th}$) The transistor is in OFF state, presenting a negligible flow of carriers.
- **Linear or ohmic mode:** (With $V_{GS} < V_{th}$) A conducting channel is formed between the drain and source terminals enabling a current called I_D to flow through, which increases linearly with V_{DS}.
- **Saturation mode:** (With $V_{DS} > V_{GS}$) the channel region sharpens towards the source contact re-emerging a depletion region near the drain, limiting I_D to a maximum value.

The MOSFET is used as the base building device in VLSI or very-large-scale integrated circuits, besides its use in power electronics circuits and radiofrequency. Nevertheless, bulk devices like the classical silicon-based MOSFET start to present performance limitations at the nanoscale because of leakage currents, channel thickness reduction, mobility reduction, power dissipation, among others [22]. Besides, such devices based on inorganic semiconducting materials are incompatible and no longer suitable for applications with biological purposes such as ours. Therefore, organic electronic devices become important and novel technologies that present dimensions approaching nanoscale and much higher carrier mobilities that reduce some limitations mentioned for silicon-based devices are also desired for such applications. Carbon-based devices such as CNTFET (Carbon Nanotube Field Effect Transistor) and GFET (Graphene Field Effect Transistor), which use carbon nanotubes and graphene as channels respectively, offer some of those characteristics.

3.2.3 Graphene

Graphene is an ideal novel material that consists of a two-dimensional honeycomb structure of arranged sp2-hybridized carbon atoms.

As a single layer infinite one-atom-thick planar sheet it has zero-band gap energy, exhibiting high mobility and low charge scattering, therefore it presents a metallic behavior [23, 24]. We use graphene for this application because it is an all-carbon highly-biocompatible material and provides a high-surface area exposed to the target molecules to be sensed.

3.2.3.1 Graphene nanoribbon

Opening a bandgap is essential in the incorporation of graphene for electronic applications and especially for its use as a channel in field-effect transistors (FETs). Several methods have been proposed to accomplish this [4]. One of them consists of the graphene being patterned along one specific direction and also its lateral dimensions being reduced, therefore a bandgap can be opened. The resulting strip is referred to as a graphene nanoribbon (GNR) and the size of the bandgap is determined by the state of

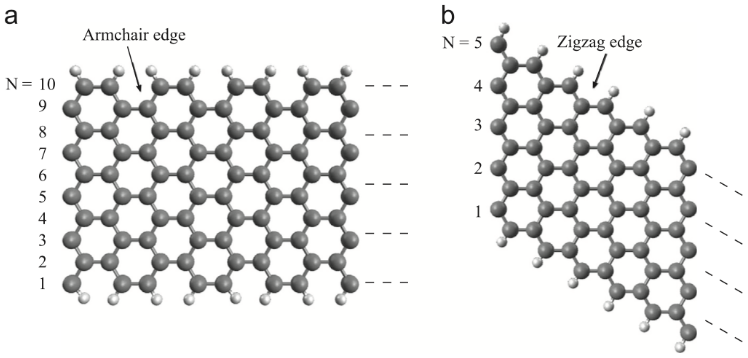

Figure 3.6: Atomic structure of a graphene nanoribbon. (a) 10-acGNR. (b) 5-zGNR. Image is taken from [5].

the edge and the width of the nanoribbon [25, 26]. There are two types of edges: armchair (acGNR) and zigzag (zGNR) (Figure 3.6). GNRs terminated in armchair edges can be metallic or semiconducting depending on their width; acGNRs with the smallest bandgap and metallic zGNRs have a width described by $N = 3p + 2$, where N is the number of carbon atoms along its width and p is an integer number. Also, experiments have shown that zGNR with narrow widths (less than 7nm) are antiferromagnetic semiconductors with bandgaps that vary from 200 to 300 meV [5].

Graphene in general is manufactured using two main techniques: top-down and bottom-up. Both have benefits and drawbacks to be considered. Top-down processes make use of etching or deposition procedures to fabricate graphene on top of a substrate, while bottom-up approaches grow the nanostructure directly on the substrate. Top-down approaches such as chemical vapor deposition (CVD), offer a low-cost option to produce graphene on large scale. However, such procedures require transferring the graphene to another substrate, which is not always an easy task, or do not have precise control over the edges (definition, roughness). Moreover, other techniques such as lithographic patterning and graphene etching present problems with the resolution obtained, which is limited [4].

On the other hand, bottom-up techniques are expected to produce well-defined edges which allow obtaining better control over the electronic properties of GNRs. This approach consists in using a precursor molecule that yields and atomically precise GNRs with different topologies and defined width and edge periphery can be obtained depending on the structure of the precursor [5]

3.2.3.2 Graphene Field Effect Transistor (GFET)

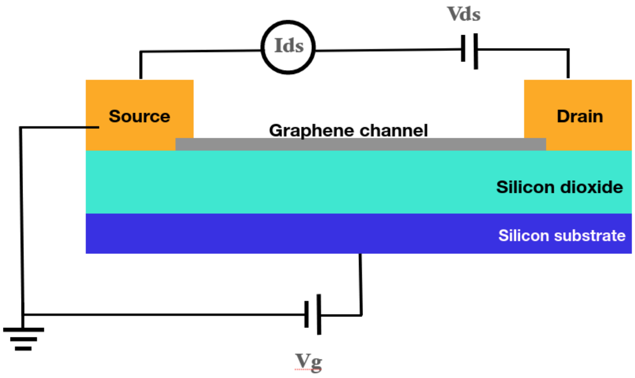

Figure 3.7: Conventional FET-based structure with graphene as a channel with a back-gate.

Due to continued miniaturization of the silicon channel on FETs and the downscaling issues, it involves, alternative options such as graphene as channel replacement arise, especially for applications requiring organic devices. Its ultrahigh carrier mobility and single-atomic thickness make it an attractive CMOS device candidate because short channel effects can be mitigated with such characteristics [4]. Figure 3.7 depicts a schematic representation of a basic GFET back-gated device.

GNRs are one option when semiconductor behavior on graphene is required for the channel junction. Smaller widths for the nanoribbon must be guaranteed to obtain such electronic characteristics. There are other techniques for gap opening which include the epitaxial growth of graphene over a substrate (i.e. silicon carbide) and they could achieve smaller widths. However, it is unavoidable to transfer graphene from the metal onto an insulating substrate for transistor device application, which might induce serious defects in graphene[27–29].

Another difference between GFETs and an ordinary silicon-based MOSFET is that the device junctions depend solely on graphene and no doping is required for electrodes, or substrate. The transport through the device and the majority of carriers will be determined by the geometry of the nanoribbons. However ambipolar behavior might be present and the majority carriers (holes or electrons) are determined by an applied electrical field from a gate voltage [30].

3.2.3.3 GFET as the sensing device

The graphene-based structures offer several advantages to be used in sensing devices, especially for biosensing applications. The main reason is because every atom in graphene is a surface atom and a possible target for reactive molecules; namely, each atom interacts directly with the sensing environment. Those interactions, to some extent, will perturb the pristine nature of the graphene structural and electronic system, being that the basis for the detection of such interaction/binding and hence allowing the detection at low-concentration of a variety of molecules [31]. Using GNRFETs, to take full advantage of the graphene's surface sensing capabilities, the channel is proposed to be a graphene nanosheet or nanoribbon, and the device with a back gate allowing the channel to be completely exposed to the environment. As an example, Akbari et. al[24], describes the detection of ammonia (NH_3) with graphene or carbon nanotube as the channel in a FET transistor. The working principle of the sensor consists of the adsorption of the gas molecule on the channel surface resulting in a change in the electrical properties (such as conductivity) of the device, the gas molecule acts as a donor. In the end, the results exhibit higher conductivity with the graphene over the CNT channel. Additionally, such a device has been used in other applications beyond the detection of gases using receptor molecules.

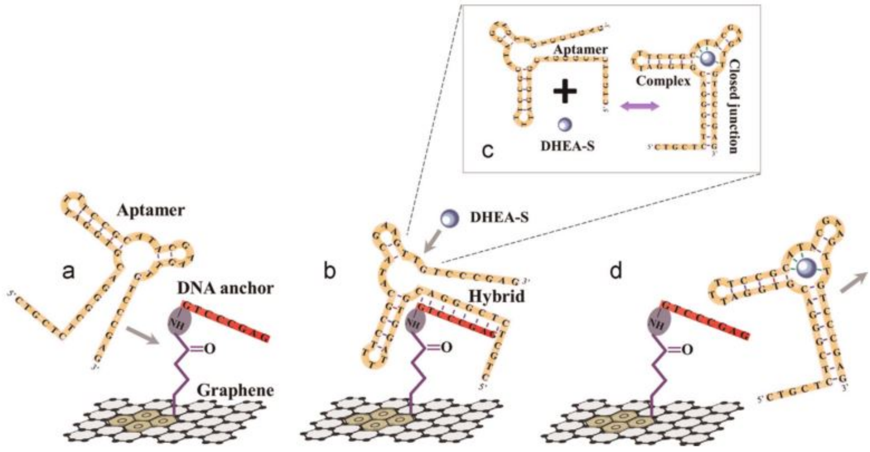

Figure 3.8: Principle of the graphene nanosensor for small molecule detection. (a) The sensing surface is prepared through complementary hybridization between the aptamer and the graphene immobilized DNA anchor. Sensing mechanism: (b) aptamer molecules hybridized to the DNA anchor can specifically bind to target small molecules (DHEA-S) in sample solution. (c) This specific binding changes the conformation of the aptamer. (d) Target molecules disrupt the aptamer–anchor hybridization, inducing the release of the aptamer from the graphene surface. Image is taken from [6].

For selectivity and enhancement of sensitivity (i.e to assure that the nanosensor only detects the desired molecule), the graphene channel could be functionalized with a specific group. For example, Wang et. al[6] describe a label-free graphene-based nanosensor for the detection of low-charged small molecules. Measuring changes in the conductance of graphene after the binding of an aptamer and an anchor, that is immobilized on the graphene, is disrupted when the analyte is introduced (Figure 3.8). Also in Green et. al[32] functionalization of graphene with aptamers and antibodies is used to bring captured antibody/ antigen complexes near the channel surface in a GFET for detection. In the same way, viruses [33], exosomes, [30] simple sugars [11], plant metabolite precursors, [12] and other types of molecules are being detected for several applications using GFETs where the graphene channel is functionalized with chemical groups called pyrenes. These are widely used because they do not affect the intrinsic electric properties of the graphene and help to stabilize and bind target molecules; this is accomplished only by conjugating a chemical group that reacts to your specific target molecule.

3.3 Computational methods

The approach used in this work to design, characterize and optimize the nanosensing device involves the use of in-silico modeling and calculation. In this section, will explain with a bottom-up approach (from quantum to classical theory), the basic theory behind the computational methods we used to carry out electronic structure calculations and dynamics simulations.

3.3.1 Quantum mechanics

Quantum mechanics allows the calculation of properties and behavior of physical systems starting from the atomistic structure and composition. First-principles quantum mechanical calculations are based on the Schrödinger equation (or approximations to it) its solution is necessary to describe the behavior of nanoscale materials, properties, and phenomena, including electronic transport.

Therefore, let us start with the non-relativistic Schrödinger equation [34], which corresponds to:

$$\hbar\frac{\partial\Psi}{\partial t} = \hat{H}\Psi \tag{3.1}$$

where Ψ is a wave function, $\hbar$ is the planck's constant divided by 2π. The Hamiltonian operator, $\hat{H}$, is the sum of kinetic and potential energy terms $\hat{H} = \hat{T}_e + \hat{T}_n + \hat{U}_{ne} + \hat{U}_{ee} + \hat{U}_{nn}$ with e and n referring to electrons and nuclei respectively [8].The first two terms of $\hat{H}$ are the kinetic energies of electrons ($\hat{T}_e$) and nuclei ($\hat{T}_n$). $\hat{U}_{ne}$ corresponds to the attractive nuclear-electron potential, $\hat{U}_{ee}$ is the electrostatic repulsion between electrons, and $\hat{U}_{nn}$ is the nuclear repulsion. $\hat{H}$ is then specifically described as:

$\hat{H} = \hat{T}_e + \hat{T}_n + \hat{U}_{ne} + \hat{U}_{ee} + \hat{U}_{nn}$

$$\hat{H} = -\sum_i \frac{\hbar^2}{2m_e}\nabla_i^2 - \sum_n \frac{\hbar^2}{2M_n}\nabla_n^2 - \sum_i \sum_n \frac{Z_n e^2}{r_{in}} + \sum_{i<j} \frac{e^2}{r_{ij}} \sum_{n<m} \frac{Z_n Z_m e^2}{r_{nm}} \tag{3.2}$$

Taking into account discrete energy levels, and considering $\Psi = e^{-iEt/\hbar}$, where E is the energy; the Equation 3.1 becomes the time independent Schrödinger equation:

$$\hat{H}\Psi = E\Psi \tag{3.3}$$

Solving this eigenfunction allows us to determine the Hamiltonian and the eigenvalues of E or energy levels and their corresponding wave functions (eigenvectors of Ψ). For practical calculations, the equation 3.3 is usually used in its discretized form, in the resulting matrix equation, the Hamiltonian is a matrix $\mathbf{H}$ with a size of $N \times N$, where N is the number of *basis functions* used to describe the atoms conforming the material structure. This Hamiltonian matrix can be obtained from first principles (ab initio methods, or from those based on an adiabatic, or Born-Oppenheimer approximation, such as Density Functional Theory explained in section 3.3.1.2), but a widely used approach is to represent it in terms of a few parameters which are chosen to match key experiments (semi-empirical methods). Semi-empirical approaches (such as Tight Binding, TB explained in section 3.3.1.3) are preferred because of their reduced computational costs and because they can often explain a wide range of experiments beyond the ones that were used as input (thanks to the reduction in complexity, which in return allows to model systems with a higher number of atoms and degrees of freedom) [8, 34].

3.3.1.1 Band structure calculation

In order to calculate the band structure of a semiconductor, a single electron is assumed to travel through a perfectly periodic lattice Equation 3.4. The wave function that describes the electron is assumed to be in the form of a plane wave moving in a specific direction with a propagation constant k, also called a *wave vector* [20]:

$$\hat{h}\Psi_{nk} = \varepsilon\Psi_{nk}(r) \tag{3.4}$$

Equation 3.5 is the space-dependent wave function of the lattice, where the eigenfunction, k, corresponds to the wave vector associated with the direction of motion of the electron in the crystal. n, corresponds to the band index [8].

$$\Psi_{nk}(r) = e^{ikr}u_{nk}(r) \tag{3.5}$$

k takes on values within the Brillouin zone (BZ)[1] corresponding to the crystal lattice. For each n and k in Equation 3.5, there will be orbital energy, o_{nk}, obtained after solving the Equation 3.4 for band n and momentum k. These resulting energies determine the band structure.

Depending on the lattice, there are critical points along symmetry directions designed names such as Γ, Δ, Z, etc and the band structure is characterized along this routes in the reciprocal space.

3.3.1.2 Density Functional Theory (DFT)

Density Functional Theory (DFT) relies on the *Born-Oppenheimer (BO) or adiabatic approximation*[35], which decouples the dynamics of the electrons and nuclei exploiting the fact that the latter are much heavier than electrons. Therefore, the nuclei positions are fixed and this allows to evolve the electrons in a field where the Hamiltonian is expressed as in equation 3.6

$$\hat{H}_e = \hat{T}_e + \hat{U}_{ne} + \hat{U}_{ee} \tag{3.6}$$

---

[1] The reciprocal lattice is divided up into cells called Brillouin zones.

However, the simplifications given by BO approximation still present a difficulty when solving equation 3.1 with the Hamiltonian from 3.6, and that is the repulsion between electrons given by $\hat{U}_{ee}$. Determining the quantum states for a N_e-electron system becomes extremely complex because it requires dealing with 3^{N_e} variables to describe the many-body wavefunction.

Here is where DFT comes, using electron density $n(\mathbf{r})$ instead of wavefunctions, reducing dimensionality regardless of N_e. The electron density is always three-dimensional independent of N_e, and this should be sufficient to obtain the ground state energy of the system[8]. The electron density for an antisymmetric wave function, satisfying the Pauli principle, can be expressed by

$$n(\mathbf{r}) = N_{\mathrm{e}} \int \left|\Psi\left(\mathbf{r}_1, \mathbf{r}_2, \ldots, \mathbf{r}_{N_{\mathrm{e}}}\right)\right|^2 d\mathbf{r} \tag{3.7}$$

where $N_e = \int n(\mathbf{r}) d\mathbf{r}$ is the number of electrons and $n(r)$ determines the probability of finding any of the N_e electrons within a 3D space $\mathbf{r}$.

DFT is derived from various contributions [8, 36]. First, the Thomas-Fermi model [37–39] introduced the use of a functional to approximate the ground state energy in terms of the electron density, although it was not the most efficient method. Later on, Hohenberg and Kohn [40] presented a theorem that proved that the electronic Hamiltonian H_e could be expressed as a functional of $n(\mathbf{r})$ and its minimization leads to obtaining the ground state energy E_G. And then using the variational principle, the Schrödinger equation can be solved.

$$E_G[n(\mathbf{r})] = \min\left\{F_{HK}[n(\mathbf{r})] + \int n(\mathbf{r}) V_{nuc}(\mathbf{r}) \mathrm{d}\mathbf{r}\right\} \tag{3.8}$$

Where the electronic Hamiltonian depends explicitly on the configuration of the nuclei only through $V(\mathbf{r})$, a given external potential and F_{HK} is a universal functional. Kohn and Sham [41] proposed to write F_{HK} as the sum of the total kinetic energy of non-interacting electrons T_s, the electrostatic repulsion energy or the Hartree energy $E_H = \int\int \frac{n(\mathbf{r})n(\mathbf{r}')}{|\mathbf{r}-\mathbf{r}'|} d\mathbf{r} d\mathbf{r}'$ and a exchange correlation energy E_{xc}.

$$F_{HK}[\mathbf{r}] = T_s[n(\mathbf{r})] + E_H[n(\mathbf{r})] + E_{xc}[n(\mathbf{r})] \tag{3.9}$$

where E_{xc} is unknown and small and T_s is determined self-consistently using the N_e single-particle Schrödinger-like equations, also called the Kohn-Sham equations expressed in equation 3.10. To this end, the noninteracting Hamiltonian $\hat{H}_{KS}$ is defined, the ψ_i are the Kohn-Sham one-electron orbitals and $v_{\mathrm{KS}}[n(\mathbf{r})]$ is an effective potential experienced by the electrons that would lead to the desired ground state density.

$$\left[-\frac{\hbar^2}{2m_e}\nabla^2 + v_{\mathrm{KS}}[n(\mathbf{r})]\right]\psi_i(\mathbf{r}) = \hat{H}_{\mathrm{KS}}\psi_i(\mathbf{r}) = \epsilon_i\psi_i(\mathbf{r}) \tag{3.10}$$

The electron density is defined as

$$n(\mathbf{r}) = \sum_{i=1}^{N_e} |\psi_i|^2 \tag{3.11}$$

and the exchange-correlation potential v_{xc} is given by the functional derivative, $\delta E_{xc}[n(\mathbf{r})]/\delta n(\mathbf{r})$

$$v_{\mathrm{KS}}[n(\mathbf{r})] = v[n(\mathbf{r})] + \int \frac{n(\mathbf{r}')}{|\mathbf{r}-\mathbf{r}'|}d\mathbf{r}' + v_{\mathrm{xc}}[n(\mathbf{r})] \tag{3.12}$$

The self-consistent procedure consists of using an initial guess for $n(\mathbf{r})$ to obtain v_{KS} through equation 3.12, then extracting the Kohn Sham orbitals solving equation 3.10 which leads to a new density obtained from 3.11. This process is repeated until a convergence criterion is achieved to finally obtain the electron density and the kinetic energy term T_s. The exact E_{xc} term is still unknown but Kohn-Sham suggested an explicit form approximation using experimental data obtained from a homogeneous electron gas, also known as Local Density Approximation (LDA) or E_{xc}^{LDA}. Improvements have been made to this approximation using not only the local uniform density $n(r)$ but also including gradient corrections, resulting in the Generalized Gradient Approximation (GGA) or E_{xc}^{GGA}. The latter being the approximation used during some quantum mechanical calculations performed during this project, which we talk about in Chapter 5.

Although DFT allows performing calculations in larger-scale systems (i.e. $N_e > 1000$) and is widely used for this reason, for electronic transport calculations in even larger systems of atoms, it becomes expensive computationally, that is why other approximations to reduce further computation times and resources are introduced, one of them being DFTB.

3.3.1.3 Density Functional based Tight Binding (DFTB)

Tight-Binding (TB) approach is used to scale down the computational cost of electronic transport properties in larger systems of atoms. This model suggests a band structure where the electrons are tightly bound to the atom to which they belong; therefore, the wave function of the system is greatly simplified as the electrons have limited interaction with surrounding atoms.

Therefore, TB enables relatively accurate results at a fraction of the cost of conventional DFT by taking the following assumptions:

1. It considers only frontier atomic orbitals 2. It considers only interactions between the frontier atomic orbitals of nearest neighbors. 3. it ignores the overlap integrals of separated atoms. 4. it may use pre-calculated parameters chosen to match the band structure of key experiments, enabling to explain a wide range of experiments beyond this used as input. [8, 34]

However, one of the problems of DFTB is that when too much strain is forced into the system the band structure changes compared to the initial state of the system, the parametrization with TB no longer truly describes the band structure of the material and starts to differ with, for example, DFT calculations results. In our system, such a strain capable of doing this would be related to higher voltages applied to the nanosensor device, therefore we avoid using higher voltages.

3.3.1.4 Landauer-Büttiker Formalism and Non-equilibrium Green's function

To describe the electronic transport properties across a device, we must introduce contacts and take them into account, meaning all kinds of entropy-driven processes. For this application, the contacts of the device span both metallic electrodes (drain and source), the gate contact, and their interaction with the semiconducting junction in the device.

Until now, the Schrödinger equation and calculation of the Hamiltonian could only describe the dynamics of an isolated channel of isolated contacts. An integration between such quantum dynamics with heat-generating processes is required to describe quantum

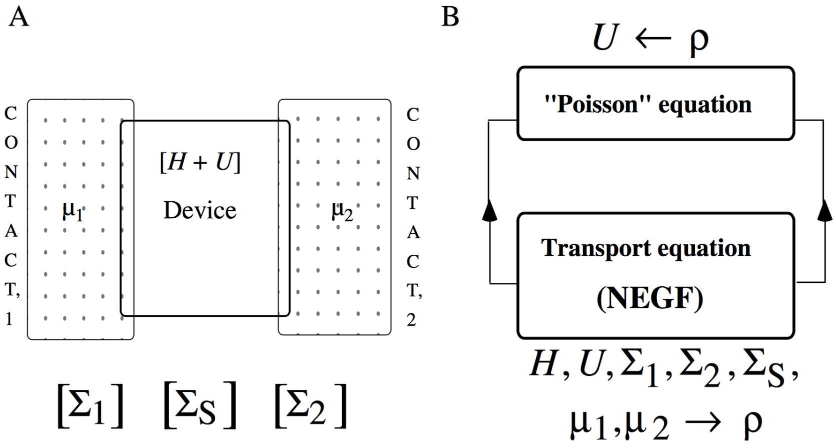

FIGURE 3.9: (A) A device driven out of equilibrium by two contacts with different Fermi levels μ_1 and μ_2; (B) self-consistent transport calculation process. Image reproduced from [7]

electronic transport. Figure 3.9 illustrates the configuration of a device, and also when a voltage is applied to the contacts. The H corresponds to the channel Hamiltonian; $[\Sigma_1], [\Sigma_2]$ are the self-energy matrices (non-Hermitian) that describe the exchange of electrons between the channel and the contacts; and $[\Sigma_s]$ is the self-energy matrix which describes the interactions of a single electron in the channel with its surroundings and is determined by "entropic forces"[5].

The Non-equilibrium Green's function (NEGF), is commonly used for the computation of quantum electronic transport in nanodevices. The general Green's equation, for non-coherent transport, includes the scattering self-energy matrix Σ_s given by Equation 3.13, which allows the calculation of free charge concentration, transmission coefficients, and current through the device (contacts included)[7][42].

$$G(E) = (EI - H - \Sigma_1 - \Sigma_2 - \Sigma_s)^{-1} \tag{3.13}$$

$$T(E) = trace(\Gamma_1 G \Gamma_2 G^{\dagger})^{-1} \tag{3.14}$$

After the Hamiltonian and the self-energy matrices are obtained from solving the Schrödinger equation (using approximations later explained in this chapter), $G(E)$ is calculated to solve the transmission coefficient $T(E)$ according to Equation 3.14, where

$\Gamma_{1,2,s}$ are the anti-Hermitian components of $\Sigma_{1,2,s}$ [42][7], hence:

$$\Gamma_{1,2,s} = i[\Sigma_{1,2,s} - \Sigma^{\dagger}_{1,2,s}] \tag{3.15}$$

Now, Landauer formalism expresses the conductance of a device with ballistic transport and the scattering processes happening within the channel in terms of a transmission probability through that channel, i.e. the previously mentioned transmission coefficient $T(E)$. And with Büttikers contribution, Landauer's formalism is generalized for a multi-terminal device [43]. Hence, the current expression is given by Equation 3.16 where f corresponds to the Fermi function $f(E)$, q to the electron charge, and $\hbar$ to the Planck's reduced constant.

$$I = -\frac{q}{h} \int T(E)[f(E, \mu_1) - f(E, \mu_2)]dE \tag{3.16}$$

After a finite bias voltage is applied to the terminals, the potential profile of the device has to be determined self-consistently by solving the Poisson equation (Equation 3.17 for the potential U and updating the Hamiltonian until a convergence criterion is reached [5].

$$\vec{\nabla} \cdot (\varepsilon_r \vec{\nabla} U) = -\frac{q^2}{\varepsilon_0} \delta\rho \tag{3.17}$$

with ε_0 the permittivity of vacuum, ε_r a spatially varying relative permittivity and $\delta\rho$ the change in the density matrix $[\rho]$. Subsequently, the density matrix $[\rho]$ is calculated from Equation 3.18, using the correlation function $G^n(E) = [A_1(E)]f_1(E) + [A_2(E)]f_2(E)$, the spectral function $A_{1,2}(E) = G(E)\Gamma_{1,2}(E)G^{\dagger}(E)$ and the Green's function $G(E) = (EI - H - \Sigma_1 - \Sigma_2)^{-1}$. This is carried out self-consistently as Figure 3.9.B pictures.

$$\rho = \int_{-\infty}^{+\infty} (\frac{dE}{2\pi}) G^n(E) \tag{3.18}$$

3.3.2 Molecular Mechanics (MM)

In quantum mechanics, the Schrödinger model and the explained approximations, make it feasible to compute quantum mechanics for smaller atom systems. However quantum methods become highly costly for larger atom systems and it becomes prohibitive to perform calculations involving dynamics calculations of the system to obtain trajectories in the order of pico or nanoseconds.

Molecular mechanics uses classical mechanics to model molecular systems. Here the resulting Potential Energy Surface (PES) obtained through the Born-Oppenheimer (BO) approximation, in the classical sense, describes the landscape over which nuclei move while under the influence of other particles (other nuclei and the ground-state mean-field of electrons); therefore this becomes useful to describe reactions, vibrations and trajectories of nuclei and consequently atoms [8].

One approximation of the quantum mechanical potential energy surface to the potential energy surface in classical mechanics is to describe the PES as a sum of simple analytical functions that are continuously derivable with respect to time, thus obtaining forces that depend only on nuclear positions. Such forces are referred to as **force fields** [8].

This approximation is mainly used in large systems of atoms that require long simulation time dynamics (pico or nanoseconds) since the potential energy of a particle, and the forces acting on it (f_i) are reduced to a function that depends on the three-dimensional nuclear coordinates (x) such as follows

$$f_i = m_i \ddot{x}_i = -\nabla_i U\left(x_1, x_2, \ldots, x_N\right) \tag{3.19}$$

where U corresponds to the before-mentioned PES, and its description can take several forms depending on the set of parameters that is used or force field [8], but in general it is described in terms of bond-dependent functions (valence), and non-bond functions as follows:

$$U = \left[U_{\text{bonds}} + U_{\text{angles}} + U_{\text{torsions}} + U_{\text{inversions}}\right]^{\text{valence}} + \left[U_{vdW} + U_{\text{Coulomb}}\right]^{\text{nonbond}} \tag{3.20}$$

where bond, angle, torsion, and angles are classical geometrical representations of atoms within molecules (Figure 3.10), and U_{vdW} corresponds to Van der Waals interactions and $U_{coulomb}$ to electrostatic interactions within a system of atoms. Van der Waals forces include attraction and repulsions between atoms, molecules, and surfaces, as well as other intermolecular forces; and the electrostatic or Coulomb potential accounts for all charged interactions between every pair of atoms flowing within a dielectric [8].

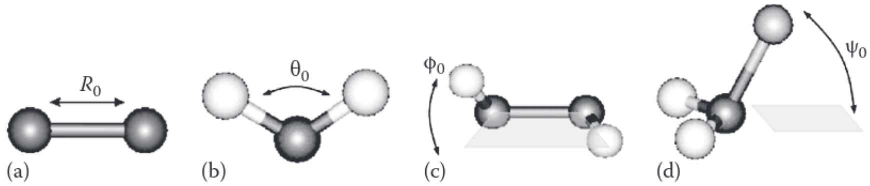

FIGURE 3.10: Classical representations of molecule structures where (a) two-body bond, (b) three-body angle, (c) four-body torsion, and (d) four-body inversion; corresponding to the valence components of Dreiding (a specific force field). Image is taken from [8]

During this project, we used a special kind of force field, a Reactive force field or REAXFF, which describes the PES in classical mechanics of a system of atoms but is optimized to accurately model the behavior of molecules where association or dissociation of new bonds during a chemical reaction would occur. This non-harmonic approximation allows us to perform a more realistic thermodynamic stability analysis, since we perform the simulation and evaluate the progress of the system through time and whether there are bond dissociation or reaction within the molecules we observe.

3.3.2.1 Molecular dynamics

Molecular Dynamics or MD simulations are performed to analyze the physical movements and interactions between a system of atoms or molecules over a fixed period of time; thus, giving an insight into the dynamic evolution of a system. It differs from energy minimization because it samples the conformational space of a system of atoms at temperatures greater than $0K$, thus allowing to model temperature and pressure effects on such a system and to measure all kinds of mechanical properties (friction, fracture, etc). In general to measure and obtain thermodynamics and time-dependent (kinetic) properties of a system of atoms.

In molecular mechanics, to obtain nuclear trajectories as a function of time and consequently, of the atoms within a system, Equation 3.19 is integrated twice with respect to time leading to those positions. The general MD simulation process is described in Figure 3.11, where we start with an initial configuration fix initial velocities of the atoms, then compute the respective forces to that set of atoms using force fields. Next, we apply a thermostat or barostat (depending on which properties of the system we fixed and

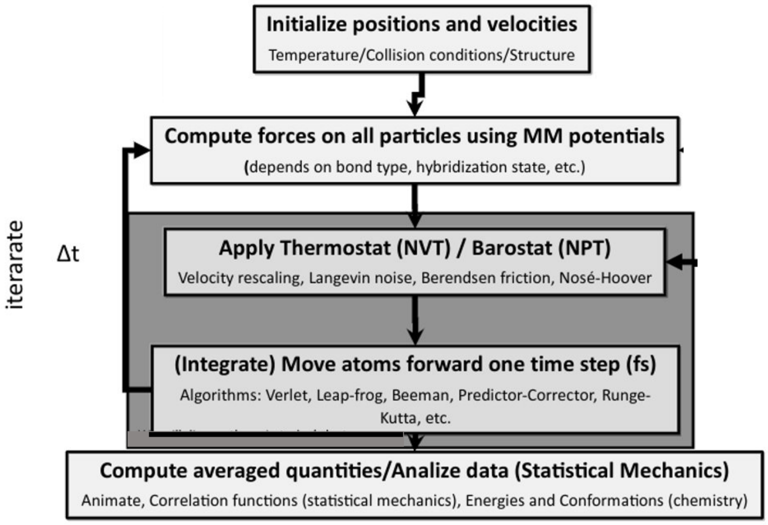

Figure 3.11: Flow chart of the molecular dynamics calculation process. Image is taken from [9]

which are we measuring i.e, energy, pressure, temperature, etc) with this we readjust velocities and integrate over one timestep to predict atoms new trajectories and iterate several times until we reach x nanoseconds or picoseconds simulations, which depend on how much time the user wants to compute.

3.3.3 Energy minimization (EM)

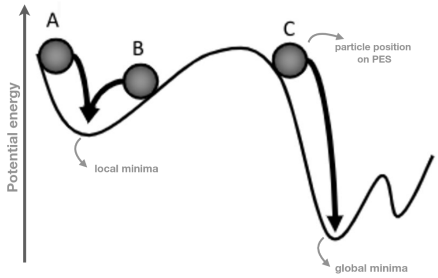

Figure 3.12: Graphic representation of energy minimization of a particle/molecule through a potential energy surface. Image reproduced from [9]

Structure refinement before starting any measurement or characterization of any system of atoms is crucial. For this purpose, it is important to perform Potential Energy Minimizations (PEM) to carry the system of atoms to a minimum energy conformation where the system is relaxed and closer to a stable structure. Minimum points on the PES correspond to stable states or geometries (arrangement of atoms) of the system [9]. Energy minimization calculations could be performed using quamtum and molecular mechanics.

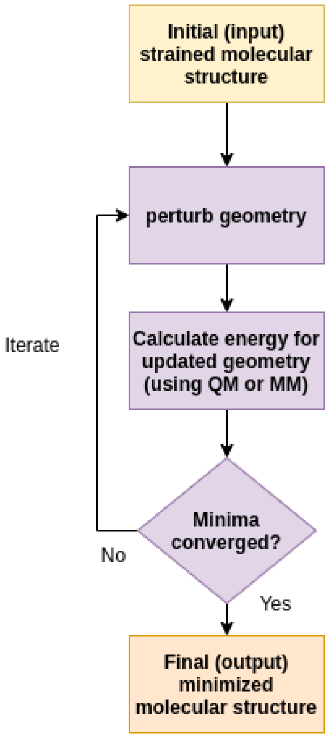

FIGURE 3.13: Flow chart of the energy minimization calculation process

Geometry minimization simulations consist of adjusting the geometric conformation of the atoms within a molecule and calculate energy and forces between those atoms until the desired RMS criteria for these two parameters is reached, i.e. the energy of the system is minimized. Several methods are used to perform minimization, for large systems with available analytical PE functions methods of first and second-order derivative methods (such as conjugate gradient or steepest descent) are preferred; for small QM systems with computationally expensive PE, and unavailable second derivatives, Quasi-Newton methods are used (such as BFGS or the limit memory version, LBFGS [44])

Chapter 4

Design of FET sensor for amylose

4.1 Amylose detection

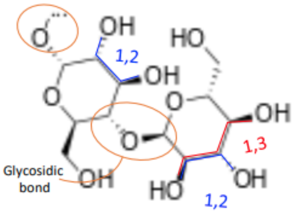

FIGURE 4.1: Amylose composed by 2 glucose units by a glycosidic bond with its respective 1,2 and 1,3-diols.

In Figure 4.1 amylose of two monomers is shown, for this application we use an extra glucose-monomer linked also by a glycosidic bond; three monomers because it is still a simple compound and this way we have a more flexible molecule and we could obtain a more thermodynamically-relaxed system than when having two monomers.

Boronic acids have been extensively used as simple sugar molecules (i.e. glucose, fructose, sucrose, etc) receptors. The reaction occurs between the boron atom and cis-diols chemical compounds present in simple sugars like glucose [45]. As amylose is confomred by glucose monomers, it presents several posible reaction spots (in Figure 4.1 1,2 and 1,3-diols present in Amylose), the reaction resulting from diol groups and boronic acids, release water molecules (Figure 4.2).

Moreover, boronic acid exists in equilibrium between the trigonal neutral or planar form with an sp^2 boron atom (Figure 4.2 top) and the tetrahedral boronate anionic form with an sp^3 boron atom (Figure 4.2 bottom) which forms in an aqueous solution and highly present under certain ph conditions (pH $>$ 9.0). An important aspect of the use of boronic acids as receptors for cis-diols chemical groups is their high dependency on the right pH conditions for their covalent binding. Yan et.al [46] propose that optimal binding should occur at a pH between the pKa[1] of the boronic acid and the cis-diol. This offers some benefits and setbacks for the purposes of the application in this project. For one instance, as the affinity and binding event chance increases between boronic acid and cis-diols when the boronic acid presents the tetrahedral form, and this form presents itself at a higher pH; this feature could be used to clean the sensor and reuse it. However, higher pH levels aren not desired for biosensing applications, because physiological pH lies around ~ 7 (although it depends on the plant), and normally higher pH solvents are needed for binding events with boronic acids. Nevertheless, the boronic acid architecture determines its pKa, therefore an evaluation of different boronic acids with lower pKa could be carried out to further guarantee the right performance of the nanosensor under physiological conditions, as Brooks et.al [47] proposes. Also, Kim et. al[45] talks about Wulff-type boronic acids that contain polymers, and how this could work at physiological pH and may be utilized as sugar-responsive materials under physiological conditions. However further evaluation of pH conditions and different variety of boronic acids lies beyond the scope of this work but could be performed.

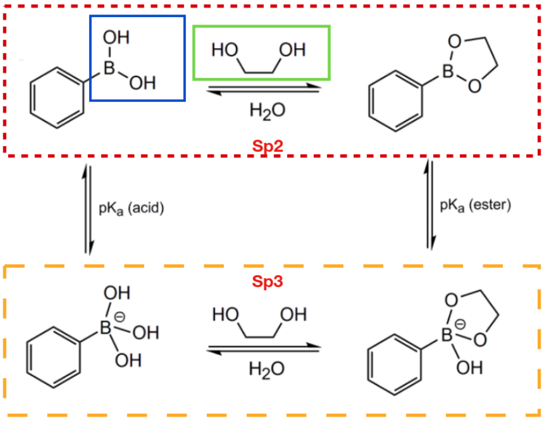

Figure 4.2: Boronic acid group (blue box) reaction with diols (green box). Red-dashed box corresponds to the sp^2 form and yellow-dashed box corresponds to the sp^3 form of the boronic acid. Image reproduced from [10]

---

[1] The pKa of a boronic acid is defined as the pH at which 50% of the boronic acid exists as the tetrahedral form [47]

4.2 Pyrene and GNR channel

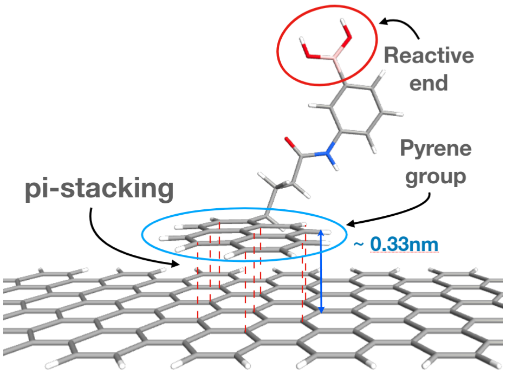

FIGURE 4.3: $\pi - \pi$ interactions between the pyrene basal plane and the graphene nanoribbon

Graphene structure presents sp2-hybridized carbon atoms which makes it prone to establish strong $\pi - \pi$ interactions [48]. This feature allows the graphene's surface and any molecule present in the environment surrounding the channel to interact. Although the presence of a molecule alone might affect the electronic properties of the channel, the target molecule in real-life conditions (i.e. physiological temperature $\sim 310K$) would constantly change its position on the channel and conformation, to avoid this and the noise it might induce into the device electronic response, we proposed to functionalize the channel exploiting the graphene's intrinsic properties such as its susceptibility to π stacking.

Therefore, we searched for molecules selective to our target molecule and also that do not affect the electronic properties of the channel so we can detect the molecule only when it binds to the receptor molecule, obtaining label-free sensing. The pyrene molecule is a polycyclic aromatic hydrocarbon that consists of four fused benzene rings, resulting in a flat aromatic system similar to the carbon atoms honeycomb arrangement in graphene. $\pi - \pi$ interactions between the pyrene aromatic base and the graphene surface allow a non-covalent way to functionalize the graphene (Figure 4.3); this interaction is caused by pi-stacking between out of plane p-orbitals on both the pyrene moiety and the GNR.

On the other end of the pyrene molecule, a specific chemical group could be bound that presents affinity to the target molecule, immobilizing it on the channel surface. The important feature of the non-covalent functionalization is that it does not perturb the pristine electronic properties of the graphene nanoribbon, allowing us to only detect something only when a molecule is attached to the reactive end of the pyrene.

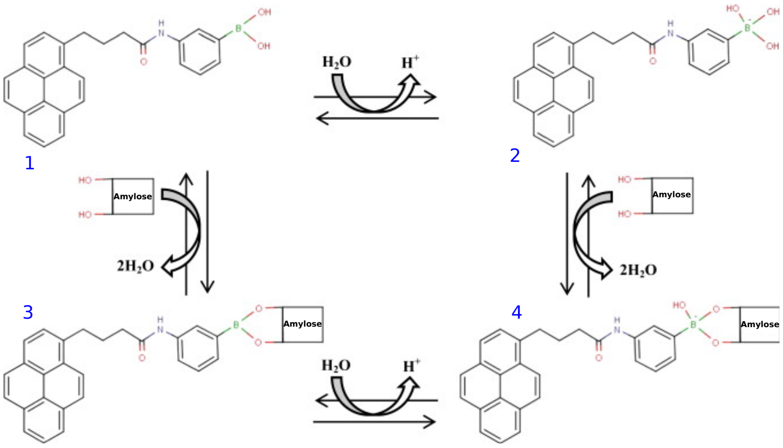

FIGURE 4.4: (3-[4-(pyren-1-yl)butanamido]phenyl boronic acid) reaction with Amylose. Image reproduced and modified from [11] .

To this end, we decided to use pyrene molecules as receptors because of their affinity and self-assembly capabilities on the graphene surface and to reactive capabilities on the other end of the molecule, also it has been extensively used on graphene-based FET sensing devices [30, 49, 50]. Therefore we use specifically (3-[4-(pyren-1-yl)butanamido]phenyl boronic acid), or PBPBA, like Wang et. al [11] use for the functionalization of a carbon nanotube channel in FETs in the detection of simple sugars. Here we take advantage of the boronic acid affinity to cis-diols in simple sugars, as mentioned before, and the pyrene self-assembly on the GNR channel (Figure 4.4).

On the other hand, pyrene butyric acid (PyBA) was also considered for the selective detection of ADP-Glucose, using the carboxylic group at one end of the pyrene to react with the amino chemical group present in the adenine of the ADP (similar as occurs in a peptide bond). More about these results in Appendix B.

4.3 Geometry of the transistor

The geometry of the transistor consists of an all-armchair graphene nanoribbon in a shape similar to a ”butterfly bandage” (Figure 4.6b), with two different widths that differentiate electrodes from the channel, taking into account the bandgap for each width as Figure 4.5 indicates. We use armchair edge ends for the entire transistor nanoribbon because it offers both, near metallic or semiconducting behavior depending on the width of the nanoribbon. This allows us to obtain a more symmetric, simpler, compact, and practical layout compared with other layouts such as using zigzag-edged nanoribbons for the electrodes and still ac-GNRs for the channel for example as Narendar et. al.[51] uses; also all-armchair could be achievable via bottom-up and top-down synthesis techniques.

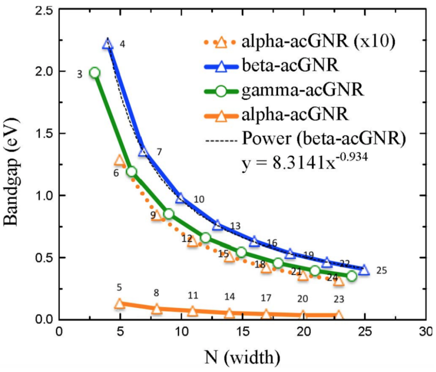

Figure 4.5: Predicted bandgaps as a function of ac-GNR width. By choosing ac-GNRs with N=11, 14, 17, 20, etc. near-metallic graphene electrodes are achieved. Calculations performed with QuantumATK using semi-empirical, extended Hückel with Cerda (graphite) basis set for C and Hoffmann basis set for H. Image taken from [12].

To determine an optimal device configuration, an in-silico screening for multiple combinations of electrodes and channel width and also channel length was performed. Based on the predicted band gaps for armchair nanoribbons as a function of their width in Figure 4.5. We chose to explore alpha ac-GNRs for the electrodes and beta-acGNRs for the semiconducting junction; higher bandgaps allow a better signal to noise ratio in GFETs while small values mean a larger signal (current capacity)[12]. Different models were used for this purpose: 14-7-14, 11-7-11, 11-10-11, and 17-10-17 (where first and last numbers of each configuration tell the electrode width W_E and the number in the middle corresponds to the channel width W_C, measured in atoms). For all configurations, the transistor counts with a back gate terminal leaving the entire GNR channel surface for sensing purposes.

The final configuration of the FET transistor consists of an 11-10-11 all-armchair graphene nanoribbon (ac-GNR), which corresponds to a $W_E = 11atoms \simeq 1.2nm$ and $W_C = 10atoms \simeq 1.1nm$ for electrodes and channel widths respectively (without hydrogen passivation). The final channel length is $L_C \simeq 6nm$ and each electrode length showed in Figure 4.6 is at $L_E = 0.85nm$ with an extension of the same size (for simulation purposes); for practical implementations, the electrodes could be longer and wider, and

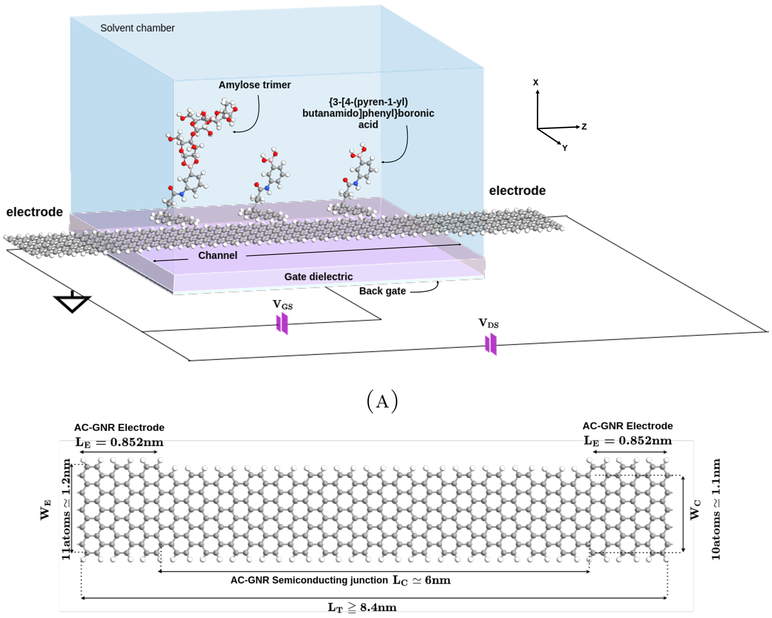

(A)

(B)

FIGURE 4.6: (A) The gnrFET sensor with solvent box in isomeric view with 3 PBPBA Self Assembly Monolayer (SAM) molecules on the channel and 1 bound trimer amylose molecule. A metallic back-gate and under the semiconducting junction a gate oxide separating region. (B) Top view of a bare optimized gnrFETs geometry and dimensions

this would not affect device performance. For the gate, we used a metallic and dielectric layer as shown in Figure 4.6a. The dielectric layer is 3.52Å wide with a dielectric constant of $4.0\epsilon_0$ corresponding to silicon dioxide (SiO_2) (and where $\epsilon_0 = 8.854 \times 10^{-12}$ and corresponds to vacuum permittivity).

The SAM layer to functionalize the GNR channel used in transport and thermodynamic simulations consists of 3PBPBAs. This maximum number of pyrene molecules on the channel was determined taking into account coverage calculations, for a channel of the same width and length, which indicate that from 4PyBAs (similar pyrene moieties) ahead, the pyrenes start to partially overlap [12]. Moreover, as the concentration of these molecules increases, the pirenes are forced to orient vertically (to achieve the highest packing density with the lowest energy) thus they stand up and stack horizontally via $\pi - \pi$ stacking leaving their edges contacting the graphene's surface [52]. Additionally, 3PBPBAs are the maximum number that can be occupied with a trimer amylose molecule, because of the size of the amylose, being a 4th PBPBA too difficult to occupy due to steric repulsion between amyloses.

Chapter 5

Characterization methods

In this chapter, we present the computational methods setup that we used to calculate the mechanical and electronic transport properties of the device and all its parts. Also, we present other calculations and protocols used to analyze the results and data obtained during and after the performed simulations.

5.1 Molecular mechanics methods

We computed molecular mechanics to model the entire molecular system at $T = 0K$ in energy minimization calculations and under $T > 0K$ in molecular dynamics. This method, allowed us to perform simulations at a very low computational cost.

Some energy minimization simulations were carried using molecular mechanics in LAMMPS [53] to consequently calculate binding energies. Hence, conjugate gradient method was used to minimize the structure geometry until a $1e-6$ RMS force or energy difference was reached. To this end, we used a specific Reactive Force Field (ReaxFF) optimized by our group, which works for hydrogen, boron, carbon, oxygen, and nitrogen (H B C O N) atoms. This force field is based on the ReaxFF for DNA [54] but optimized for Boron-Carbon and Boron-Oxygen interactions.

5.1.1 Molecular dynamics simulations

Molecular Dynamics (MD) calculations were also carried out in LAMMPS, using the aforementioned ReaxFF force field along with the charge equilibration method (Qeq) [55], in parallel high-performance computer nodes. All structures were prepared in vacuum using Quantum ATK molecule editor and solvated explicitly, using Packmol package [56], with water molecules to a density of 1g/cc and Potassium (K) counterions to achieve a net-neutral system charge since we used the tetrahedral sp^3 form of PBPBA. The number of counterions is determined by the number of PBPBAs since each one presents a charge of -1, being one counterion for each ligand.

For these MD simulations we followed the process of: first, the structure geometries were minimized using a conjugate gradient method to an RMS force or energy difference of $1e-7$. Then we introduced temperature to the system by performing a ramp of temperature from $0K$ to $300K$ to consequently equilibrate the system at $300K$. To this end, an ensemble of initial velocities for all atoms is generated; corresponding to a Gaussian distribution scaled to produce the initially requested temperature of the system (i.e. 10K). Besides, we perform time integration on a Nose-Hoover thermostat [57](Nose-Hoover style non-Hamiltonian equations of motion) using an NVT canonical ensemble (fixed temperature) over 1 or 2 nanoseconds. The timestep used was 0.5 femtoseconds along with a damping factor of 50 femtoseconds. This thermostat allows us to update the position and velocity for all atoms in the system each timestep, taking into account the desired temperature.

We used MD simulations, to evaluate the evolution of the system at room temperature conditions in the simulations that involved the amylose alone on the GNR channel and PBPBAs alone over the GNR channel. For the simulation of the PBPBA and the linked amylose, after running equilibrium, we heated the system even more through a ramp in temperature from $300K$ to $350K$, to further evaluate the thermodynamic stability at physiological temperature $\sim 310K$, and see what happens with the ligand molecule, if the van der Waals hold it enough or it detaches from the GNR channel; also what happens with the amylose trimer, if it still stands or physisorption[1] on the graphene happens.

---

[1] Physical adsorption that happens by van der Waals forces

Furthermore, MD calculations were carried using a fixed graphene in the x direction (direction perpendicular to the graphene surface and the transport direction) since free-graphene at room temperature presents thermal-induced fluctuations and no longer maintains a static planar form (moving in the x direction). Therefore, we fixed the x position of the graphene nanoribbon (since we were simulating the channel junction, and the graphene is supposed to be placed over a substrate) setting its velocities and forces along the x direction to zero so the GNR does not move along x but letting it move in y and z direction.

5.2 Quantum mechanics methods

Quantum mechanical calculations for energy minimization needed in binding energies calculations rely on solving the Schödinger equation as we mentioned in Chapter 3. Thus, were carried out these calculations using Density Functional Theory (DFT) [58] as implemented in QuantumATK package [59][60]. Here, the Kohn–Sham Hamiltonian is expanded into a numerical Linear Combination of Atomic Orbitals (LCAO), Quantum ATK comes with pre-built basis sets of orbitals that represent each chemical element for different pseudopotentials. For the exchange-correlation parameters, we used Generalized Gradient Approximation (GGA) Perdew-Burkey-Ernzenhof (PBE)[61] pseudopotentials Fritz-Haber Institute (FHI) [1] code with Double Zeta Polarized (DZP) basis sets.

All DFT calculations included London dispersion corrections (Van der Waals corrections important for the interaction between the graphene and the pyrene base), at the Grimme D3 level[62]. Before any binding energy or transport calculation were performed, all structures simulated were minimized using LBFGS [44] method as implemented in QuantumATK package to a convergence max forces criteria to $0.05eV/\text{Å}$.

Furthermore, for device electronic transport calculations, some quantum mechanics calculations were carried using Density Functional Theory (DFT)[58] (See Appendix A) but it is too computationally expensive therefore we decided for Density Functional based Tight Binding (DFTB)[63] methods. These are coupled to the non-equilibrium Green's Functions (NEGF) machinery [64], as implemented in Quantum ATK [60].

For the Hamiltonian calculation in 14-7-14[2] configuration, we used DFTB with CP2K (integrated in the ab initio code CP2K [65]) parameter set and Slater Koster basis set. For Electronic transport from 11-7-11 configuration and there on we used also DFTB, Slater Koster with the parameter set Magsil-1-1 [66]. We also performed some simulations of electronic transport with Extended Hückel [67] however it was more expensive since it required higher sampling the Brillouin zone and did not continue with this method (More about this and methods comparison in Appendix A).

For minimization and transport calculations, self-consistent iteration was enabled, using the Pulay mixing scheme (PulayMixing Algorithm [68]) to obtain the best guess for the next input (to a hamiltonian variable). Energy convergence criteria for minimization was $1e-5$ and a damping factor of 0.1. In the case of transport calculations, energy tolerance was $5e-5$, and the damping factor we varied (using 0.1 or 0.05) to reach convergence in some voltages.

A Multigrid Poisson solver with a Periodic boundary condition in A and B direction and a Dirichlet boundary condition in the C transport direction was used. For numerical accuracy parameters, we used a Monkhorst-Pack grid with 101 k-points in the C direction (transport direction), for a good sampling in the reciprocal space when using Slater Koster. Also to indicate the periodicity of the electrodes only in this direction.

The self-consistent energy calculation for a device (with electrodes) is first performed to obtain the Hamiltonian for each of the electrodes under periodic boundary conditions. Then the self-consistent calculation for the central region is performed with open boundary conditions using the self-energies calculated from each electrode. Electronic transport calculations did not include the effect of a solvent (explicit or implicit) different than vacuum.

5.3 Analysis protocol

5.3.1 Binding energy

In order to ensure that the target molecule has correctly bound to the pyrene ligand, we calculated the binding energy of the resulting complex. The binding energy is defined

---

[2] Explanation for this nomenclature in Section 4.3

as the minimum energy required by a particle to dissociate from a system of particles. In this case, the binding energy would be the minimum energy required by the target molecule to dissociate from the pyrene ligand. The formula is given by Equation 5.1.

$$E_{bind} = E_{system} - (E_{pyrene} + E_{targetmolecule}) \tag{5.1}$$

Thus, in order to have binding energy, the resulting energy value after the complex is bound (target molecule bound to the pyrene ligand) needs to be smaller than the respective energy values corresponding to the separate molecules, i.e. we have binding energy when $E_{system} < E_{pyrene} + E_{targetmolecule}$. Binding energies were calculated with the system an it's separate molecules in vacuum and after performing energy minimization for each part (i.e. pyrene, target molecule, complete system)

5.3.2 Physisorption energy

Similar to binding energy, the physisorption energy was calculated to measure the stabilization induced by the $\pi - \pi$ interactions that are present between the graphene's surface and the pyrene moiety aromatic base. We calculated this energy using Equation 5.1 too. Thus, $E_{system} < E_{acGNR} + E_{pyrene}$ must be fulfilled to obtain physisorption energy.

5.3.3 Thermodynamic stability of PBPBA

Binding energy calculations only ensure the stability of the compound under ideal conditions, vacuum, and at zero Kelvin. In order to further guarantee that the docked molecules (amylose and PBPBA) are stable, the final compound must be subjected to more close to reality conditions such as physiological temperature. Therefore, we ran reactive MD simulations to observe how the system evolves over a period of time and used a force field as a computational method, here the bound complexes underwent $300K$ temperature conditions for 1 or 2 nanoseconds in order to observe the thermodynamic stability of the system.

Using the resulting coordinates in the MD trajectory, the center of mass (COM) was calculated for the acGNR atoms and the pyrene basal plane atoms.

$$COM_x = \frac{\sum_i m_i x_i}{M} \quad COM_y = \frac{\sum_i m_i y_i}{M} \quad COM_z = \frac{\sum_i m_i z_i}{M} \tag{5.2}$$

Where COM for each coordinate, and M and m_i are the total mass of a group of atoms and the atomic mass of the i-th atom, respectively. We were mostly interested in changes in the difference between COM_x of acGNR and the PBPBA.

5.3.4 Electronic transport properties

First, we evaluated the electronic transport properties starting from the *band structure* of each junction of the device separately, electrodes, and channel. For electrodes, we look for near to zero bandgaps and for semiconducting channel junction a bandgap around $E_g \sim 1eV$ looking for a bandgap close to Silicon $E_g = 1.12eV$, as the most commonly used semiconductor. To this end, we measured the difference between the HOMO and the LUMO bands.

Next, we simulated the transistor electronic properties at zero drain-source bias, namely when the transistor is in equilibrium state. At zero drain-source and gate bias, we observed the Fermi level of all the junctions (electrodes and channel) is in equilibrium, here we observed whether there is a deviation of the Fermi level if is closer to the HOMO band, presenting a tendency for positive gate voltages; conductance is dominated by holes i.e. the transistor behaves like a p-type. What that means, is that the electrode with the highest temperature will have the most holes, propagating this type of carrier to the other electrode giving rise to a current in this direction. Or on the contrary, if the Fermi level is closer to the LUMO band, is n-type and conduction dominated by electrons in equilibrium state.

When a bias voltage is applied to the electrodes of the ac-GNR FET device, this gives rise to a shift in the Fermi levels of each electrode given by $-eV_{DS}$. When there is a difference between the left and right chemical potentials μ_L, μ_R of one electrode respective to the other, there is flow of electrons. For example, if left electrode has a higher electrostatic potential than the right electrode, electrons flow from the left to the right, and since conventional current is made by holes, that corresponds to an electrical current from right to left. Gate voltages are used to modulate

QuantumATK applies NEGF equations for the device's electronic transport calculations. For applied drain-source and gate voltages and different electrode temperatures, the self-consistently calculation of the non-equilibrium density matrix is carried out and from it, it is possible to calculate other transport properties one of them being the transmission spectrum. Transmission spectrum contains the transmission coefficients and applying Landauer-Büttiker Formalism (Section 3.3.1.4) the conductance and consequently, the current of the device is calculated.

5.3.5 Sensor properties

Besides evaluating the electronic response to the final device we calculated other properties to characterize the detection limits of the sensor.

5.3.5.1 Limit of detection

The Limit of Detection or LOD corresponds to the minimum quantity of analytes that the sensor is capable to detect in a given nano-array consisting of a number n of nodes, where each node consists of a FET as the one ac-GNR proposed in this work.

$$LOD = \frac{1}{(Vol_{eff} \times N_A)} \times \frac{1}{n}$$

Being Vol_{eff} the effective solvent accessible volume in Liters (corresponding to the solution chamber in Figure 4.6a) and N_A Avogadro's number [3].

We described sensitivity in terms of the LOD, with a nano-array consisting of n nodes, to more nodes a lower value of LOD is obtained and with this more sensitivity of amylose.

---

[3] The number of atoms or molecules in one mole

Chapter 6

Results of characterization and discussion

In this chapter, we present the results for the design and characterization of the models presented in previous chapters.

6.1 Thermodynamics

6.1.1 Binding of the target molecule and pyrene ligand

We calculate the binding energies for two possible target molecules, which could indirectly detect starch: ADP-Glucose and Amylose. Amylopectin was discarded due to its molecular size and its highly branched nature. The first option was ADP-Glucose using Pyrenebutyric Acid (PBA) as the receptor on the channel and results for that matter are in Appendix B.

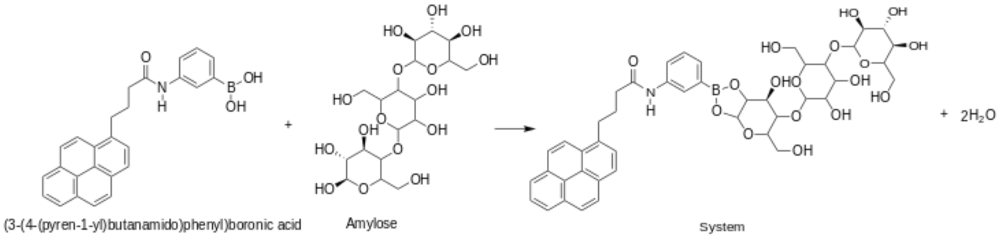

FIGURE 6.1: Schematic diagram of amylose and PBPBA reaction. The PBPBA boronic acid end reacts with one 1,2 diols of one the external glucose-monomers of the amylose and releases 2 water molecules

As mentioned earlier, amylose is a polysaccharide and its glucose chain length varies depending on the plant variety, maturity, etc, so we fixed length to 3 glucose monomers and assume binding takes place on one end of the chain (as in Figure 6.1. For a ligand, we use (3-[4-(pyren-1-yl)butanamido] phenylboronic acid) or PBPBA, as mentioned in the previous chapter and as Tlili et al. [11] use in their sensor.

Using DFT and REAXFF, we performed geometry minimization of each of the parts (as in Figure 6.1) and thereafter compute the binding energy as shown in Table in6.1, using the method described in Chapter 5.

	FHI-DZP (DFT)	**ReaxFF**
$\mathbf{E_{bind}}$	-18.551 kcal/mol	-19.114 kcal/mol

Table 6.1: Binding energies for Amylose molecule and PBPBA in Sp^3 hybridization

The binding energy between PBPBA and amylose is consistent in both methods and with it the affinity of the ligand to our target molecule. The consistency of REAXFF with DFT results also confirms the accuracy of the force field.

Furthermore, the preference of amylose as target molecule over to ADP-Glucose is because binding energies for the latter are $3kcal/mol$ lower (See Appendix B for ADP-results); comparing the best location in amylose to bind with PBPBA (between 1,2 cis-diol in amylose and boronic acid in PBPBA) and the best location in PBA to bind with ADP-Glucose (between the carboxylic group in PBA and the amino group in ADP-Glucose). Moreover, amylose corresponds to a molecule biologically available outside cells, while ADP-Glucose is an intracellular molecule, therefore we preferred the former.

6.1.2 Physisorption energy of the PBPBA and graphene

Similarly, physisorption energy calculations for the PBPBA on the acGNR semiconducting junction were computed. This, using the same approach as in binding energy with Equation 5.1. As we can see in Table 6.2, even when the interaction between the PBPBA and the graphene nanoribbon does correspond to a non-covalent type, the interaction and physisorption between pyrene and GNRs are clear, as experimental [11, 30, 33] and other in-silico works [12, 52] have proven.

	DZP (DFT)	**ReaxFF**
$E_{physisorption}$	-49.65 kcal/mol	-37.29 kcal/mol

Table 6.2: Physisorption energies for bound amylose and PBPBA, on a graphene nanoribbon

As Table 6.2 indicates, there is good physisorption energy, indicating that the PBPBA is attracted to the acGNR through strong interactions that will provide stabilization to the amylose on the FET channel. ReaxFF calculations are also consistent with quantum mechanics, with resulting physisorption energy close to DFT calculations, which confirms the accuracy of the force field too.

6.1.3 Ligand-analyte stability under physiological conditions

To confirm the thermodynamic stability of the ligand-amylose on the semiconducting channel, we performed reactive molecular dynamics (MD) of the system over several nanoseconds and a temperature range of $290 - 360K$ measuring changes in the position of the center of mass for each molecule in the system.

6.1.3.1 Graphene nanoribbon with amylose molecule alone

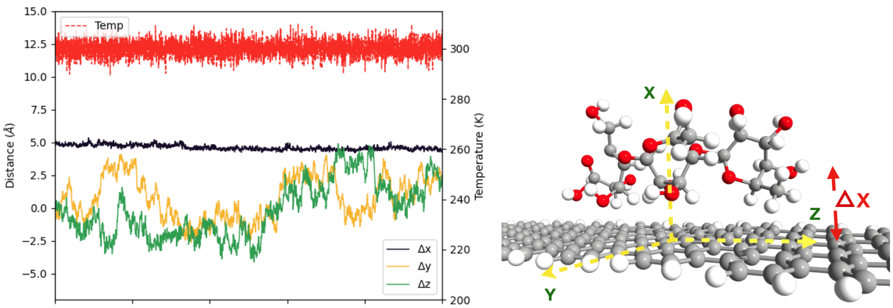

(A) (B)

Figure 6.2: (A) Difference in x, y, and z coordinates between acGNR's semiconducting junction part and an amylose molecule (B) Amylose on graphene channel. The origin of the coordinate system is at the center of the GNR

MD simulations for 1 nanosecond in thermodynamic equilibrium (with sustained temperature around $\sim 300K$) were carried out for an amylose trimer molecule over an acGNR length of 47Å. Figure 6.2a depicts the difference between the centers of mass of the amylose and the graphene (the center of mass of the GNR is located at the origin of the coordinate system). The position of the center of mass of the amylose in x-direction varies from a minimum of 4.19Å to 5.34Å. Also for the position in the y-direction (along the width of the acGNR), we observe that the amylose alone varies its position constantly.

6.1.3.2 Graphene nanoribbon ligands

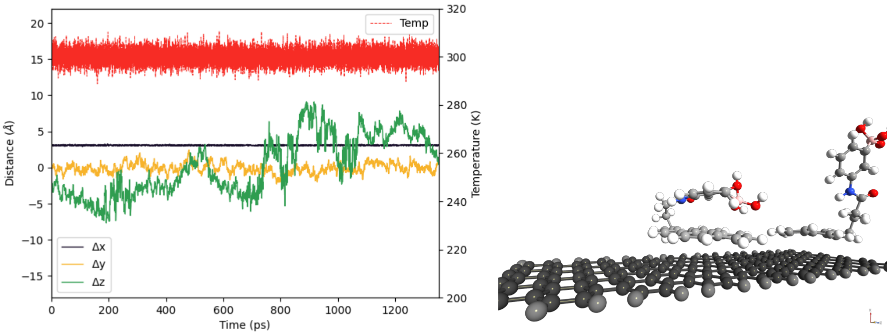

(A) (B)

Figure 6.3: (A) Difference in x, y, and z coordinates between acGNR's semiconducting junction part and pyrene basal plane (B) PBPBAs on an ac-GNR

MD simulations for 1.4 nanoseconds were also carried for two PBPBAs on the acGNR channel. Position of the pyrene groups (in the PBPBA) in the x direction varies between 3.25Å and 2.89Å (Figure 6.4), which confirms the physisorption of the pyrene base on the graphene surface even at room temperature, and this distance also is consistent with the distance reported in other works with pyrene moieties [12] and with experimental interlayer distance between graphene sheets in graphite (∼ 3.4Å). With a low concentration of PBPBAs on the graphene nanoribbon, they have enough space to move around along y and z directions, being expected as they mainly interact with the surface of the graphene [52].

6.1.3.3 Graphene nanoribbon with a ligand and amylose

MD calculations were also carried out for one PBPBA linked with an amylose trimer over an acGNR surface. A nanoribbon of shorter length was used, 34Å for this simulation, due to the increment of the number of atoms (because of the explicit solvent) and the computational cost that it implies. The position of the pyrene base (with the PBPBA and amylose linked) in the x-direction varies between 3.62Å and 2.89Å, maintaining that range even when the temperature increases from 300K to 350K. Position in the z-direction varies constantly along the nanoribbon and especially for the last ramp of temperature to 350K, however, the pyrene base maintains it physisorption state on the surface remaining also linked to the amylose.

Furthermore, during the thermodynamic equilibrium in the first part of the plot in Figure 6.4a, we observed that the benzene group in the PBPBA also ends physisorped on the graphene's surface and remains in that form (Figure 6.4b), which means that the PBPBA can further stabilize the amylose, reducing the mobility of the pyrene end and consequently immobilizing further the analyte.

An amylose trimer presence on the semiconducting junction (As depicted in Figure 6.2b without a ligand) could induce a shift in electronic transport through the device. However, the resulting electronic signal might present a lot of noise that comes from the constant shifting of amylose position, rotation, and conformation with respect to the graphene's surface (i.e. thermal-induced noise that later is reflected in the electronic response). On the other hand, if we use PBPBA as a receptor molecule for the amylose, we stabilize the position of the amylose in the sense that the pyrene moiety always faces the graphene surface and interacts with it, and how the amylose binds to the PBPBA is not relevant for it to affect the intrinsic electronic properties of the device.

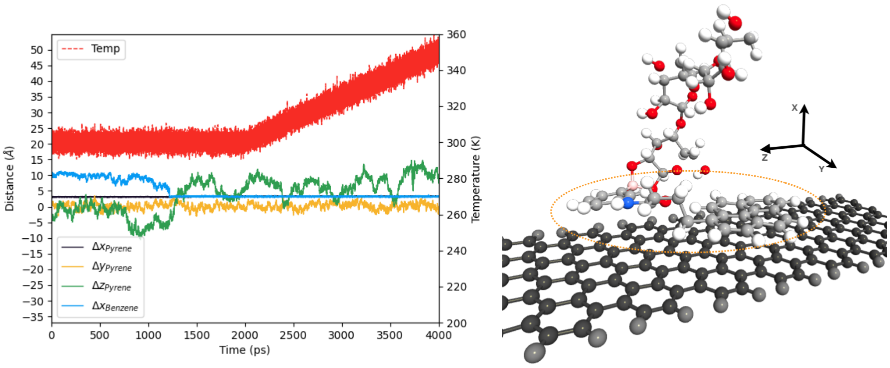

(A)

(B)

FIGURE 6.4: (A) Difference in x (black), y (yellow) and z (green) coordinates between acGNR's semiconducting junction part and pyrene basal plane; also difference in x (blue) between the benzene group in the PBPBA and the GNR, and red dots correspond to temperature. (B) Linked amylose to a PBPBA, where pyrene ligand seems completely physisorped (dashed circle) on the GNR semiconducting junction

6.2 Transport properties

6.2.1 Models

We evaluated different combinations of arm-chair widths for the electrodes and channel observing type of transport (thermionic or tunneling-driven), conductance through the channel, on-off ratio of the current. For the first, we studied the conductance through the device as we varied the electrode temperatures from 0 to 1000 Kelvin alongside the gate voltage. We present and explain these results next.

6.2.1.1 14-7-14 acGNR

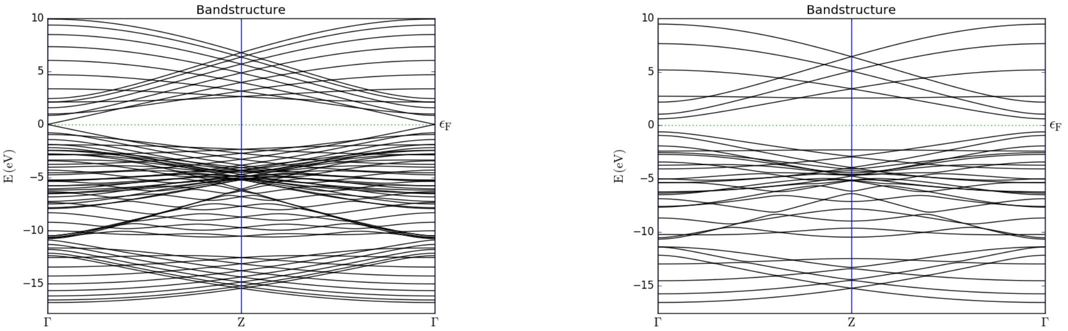

(A)

(B)

Figure 6.5: (a) Bandstructure for 14 and (b) 7 atom width acGNR nanoribbon configuration. Bands are plotted in terms of their energy vs the Brillouin zone route (i.e. Γ, Z as critical points in the route).

Electrodes of 14 atoms of carbon wide, present a bandgap of $0.0279eV$ presenting a near-metallic behavior, on the other hand, a channel of 7 atoms wide with a bandgap of $1.2234eV$ correspond to a semiconducting behavior. For this configuration, we evaluated different channel lengths: 4.3, 5.1, and 6 nanometers long. Figure 6.5 shows the corresponding band structure for both widths, where the bands are plotted in terms of their energy and the Brillouin zone points for which we calculated the band structure.

Figures 6.6 depict the respective conductance vs gate voltage plots for the different channel lengths. For instance, in the device with the shorter channel length at 4.3nm in Figure 6.6d, we observe that the conductance is dominated by tunneling transport (no temperature effect) at the red shadowed window and also a high dependency on the gate voltage. On the other hand, the following length of 5.1 nm in Figure 6.6e, presents a

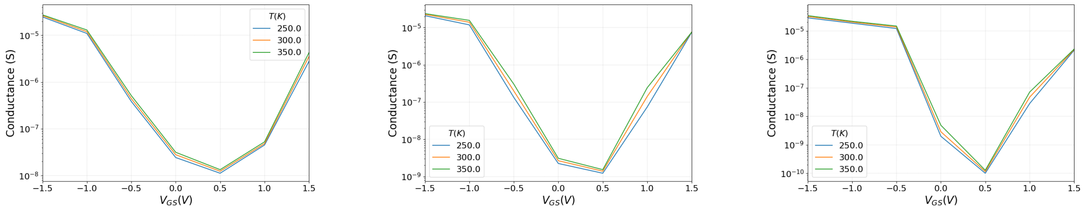

(A) 4.3 nm (B) 5.1 nm (C) 6.0 nm

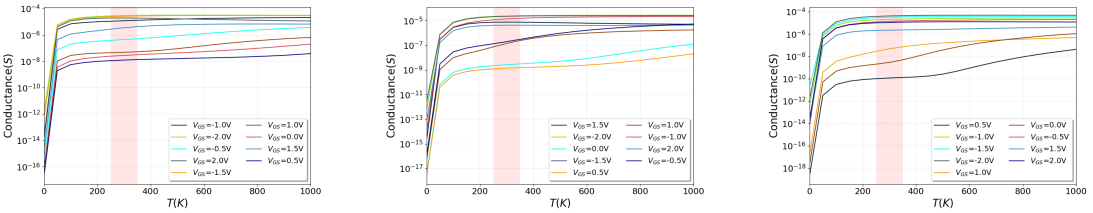

(D) 4.3 nm (E) 5.1 nm (F) 6.0 nm

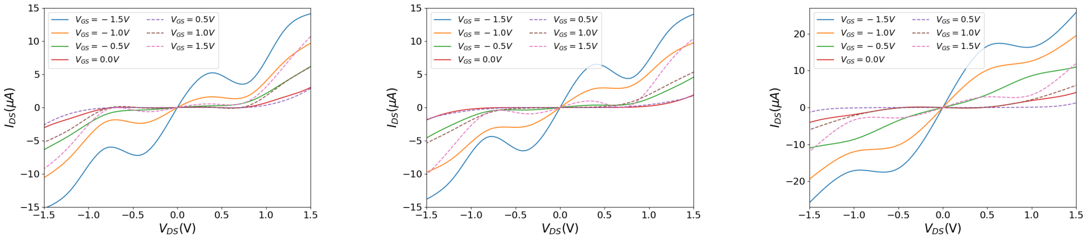

(G) 4.3 nm (H) 5.1 nm (I) 6.0 nm

Figure 6.6: (A-C) Conductance plots for different channel lengths in 14-7-14 acGNR nanoribbon configuration, (D-E) Conductance vs Temperature, the red-shadowed region corresponds to $T = [250 - 350]K$, the working temperature window of the device.(G-H) Are IV characteristics plots. Each column corresponds to a channel length, 4.3, 5.1, 6.0 nanometers respectively

slope for $V_G = -0.5V, -1.0V$, where conduction has a slight dependence of temperature at this voltages, although the rest of the gate voltages show a clear tunneling transport. And for the channel length of 6nm, (in Figure 6.6f) the device has tunneling transport in all gate voltages except maybe for $V_G = 0.0V, 1.0V$ (within the red-shadowed zone). In general, for the operational temperature window, we observe that the conductance in all lengths presents a higher dependency on the modulation of the gate voltage and temperature has only a small effect on transport, which indicates predominant tunneling over thermionic transport. We select the geometry that leads to higher conductance and almost no effect of temperature, namely thermodynamic stability is critical in the operation region of the device.

Also in Figures 6.6d-6.6f the minimum value for the conductance is around $V_G = 0.5V$, which corresponds to a shift of the Fermi-level due to the electrochemical potential of the electrodes. That means that for this geometry, 14-7-14, the valence band (HOMO) is closer to the Fermi Level when the transistor is in equilibrium (zero bias) towards positive gate voltages, indicating that transport is dominated by holes at equilibrium.

We notice that as the channel length increases, the device presents a larger current response. Conduction type does not change because this feature is intrinsic of the geometry of the junctions (i.e. 14-7-14). The increment in conductance, and consequently in current through the device, is easy to see from Figure 6.6g-6.6i and is a function of the available density of states (DOS). For this reason and also taking into account the results in previous works [12] where similar lengths are used, we decide thereon to use a channel of 6nm long.

Nonetheless, although 14-atom wide electrodes present a near-metallic behavior, we decide to decrease electrode width seeking to reduce the number of atoms in the device for computational cost, albeit maintaining a near-zero bandgap.

6.2.1.2 11-7-11 acGNR

Consequently, we use electrodes of 11 atoms carbon wide, that present a bandgap of $0.05eV$ presenting a near-metallic behavior and using the same width of 7 atoms wide for the semiconducting junction for the $6nm$ long channel. In Figure 6.7 we show the respective conductance plots for a transistor with these two junctions.

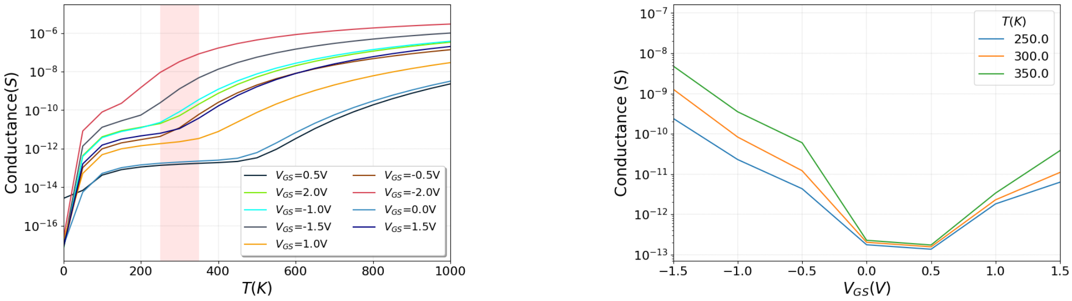

(A) (B)

Figure 6.7: (A) Conductance through channel vs Temperature in electrodes and (B) Conductance vs gate voltage for 11-7-11 acGNR nanoribbon configuration

Figure 6.7a portrays a stronger thermionic effect compared with the results for the previous device. Here, all the gate voltages present a larger slope in conductance in the temperature range of $T = [250 - 350]K$, and especially for negative values, meaning greater conductance through the channel for these gate voltages where we found great thermal dependency. Only gate voltages $0.0V < V_{GS} < 1.0V$ show some thermal stability in the shadowed zone but with clearly lower conductance values.

The effect of temperature is also confirmed in Figure 6.13b, where is easy to distinguish how the conductance increases substantially for 350K compared to the 250K line plot. Therefore, if this device is to be used for the sensor, we would take $V_{GS} = 1.0V$ as working voltage for the device.

On the other hand, in the same figure, we observe a deviation when the transistor is at zero gate bias towards positive gate voltages, meaning a hole-dominated transport for this device.

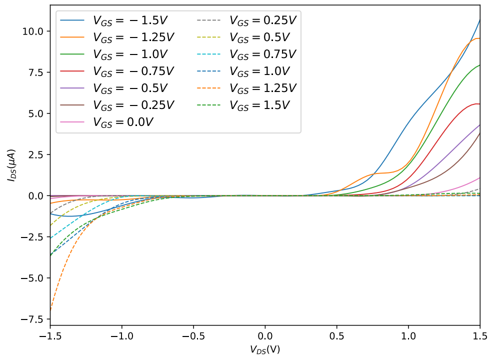

FIGURE 6.8: IV plot for configuration 11-7-11

Nevertheless, comparing this device with the 14-7-14 we observe that not only thermionic transport is predominant here, but also control by gate voltage reaches lower conductance values compared with the previous device. That could be seen too in Figure 6.8, where higher values of drain-source current go around $\sim 10\mu A$ compared with $\sim 26\mu A$ in 14-7-14.

Moreover, a channel width of 7-atoms or 7.38Å is just too tight for a pyrene moiety of 5.36Å × 6.22Å (for the pyrene base without edge passivation) to fit in. So we decided to try different geometries where we increased the atom width of the channel to 10-atoms taking into account its predicted semiconducting behavior.

6.2.1.3 17-10-17 acGNR

A configuration conformed by 17 atoms wide with a corresponding bandgap of $0.0214eV$ for the electrodes corresponding to the smallest value we obtain until now (Figure 6.9a);

also a 10-atom wide channel ($6nm$ long) was considered, where this acGNR width presents a bandgap of $0.9108eV$ (Figure 6.9b), for semiconducting behavior.

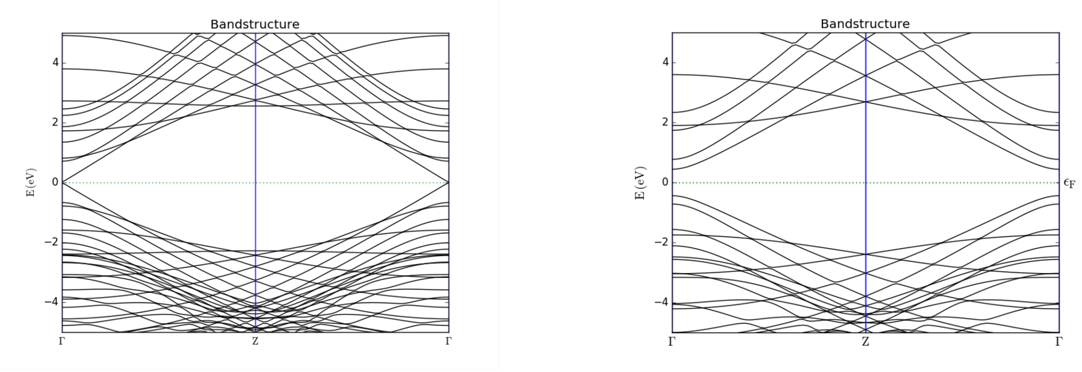

(A)

(B)

FIGURE 6.9: (a) Bandstructure for 17 and (b) 10 atom width acGNR nanoribbon configuration. Bands are plotted in terms of their energy vs the Brillouin zone route (i.e. Γ, Z as critical points in the route).

Figure 6.10a shows higher conductance values for the device and also showing almost no temperature dependency between 250K-350K (red-shadowed area) across all gate voltages; here we could use any gate voltage value except maybe for $V_{GS} = 0.0V, 0.5V$ that present the lowest conductance values. Regarding the type of conduction, Figure 6.10b shows the deviation of the conductance plot towards positive gate-bias when the device is in equilibrium, which indicates p-type conduction in this state as previous devices.

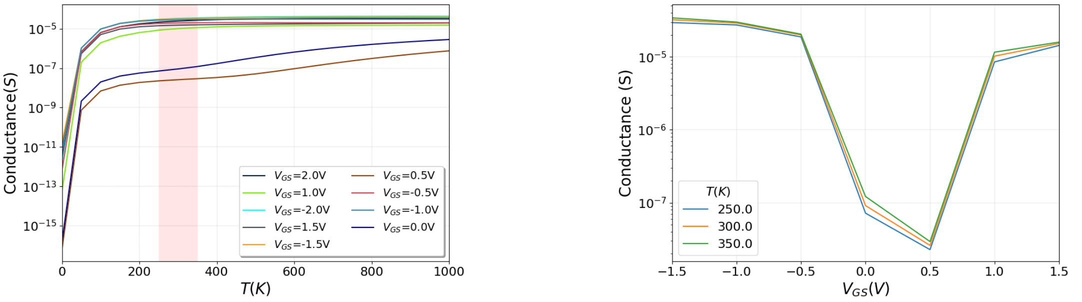

(A)

(B)

FIGURE 6.10: (a) Conductance vs Temperature in electrodes and (b) Conductance vs gate voltage for 17-10-17 acGNR nanoribbon configuration

By analyzing Figure 6.11, where we performed IV characteristics only for positive gate voltages however giving us enough insight into the device's transport capabilities; here the resulting high output current capabilities of the device are consistent which the device geometry taking into account that the 17-atom width electrodes allow higher carrier injection into the channel.

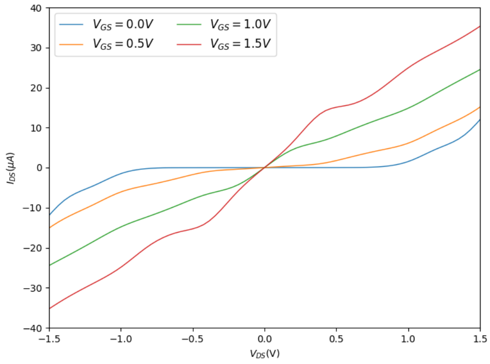

Figure 6.11: Drain Source Current vs Drain Source Voltage (IV plot) for configuration 17-10-17

However, we decided to try smaller electrode widths to decrease the size and number of atoms of the device.

6.2.1.4 11-10-11 acGNR

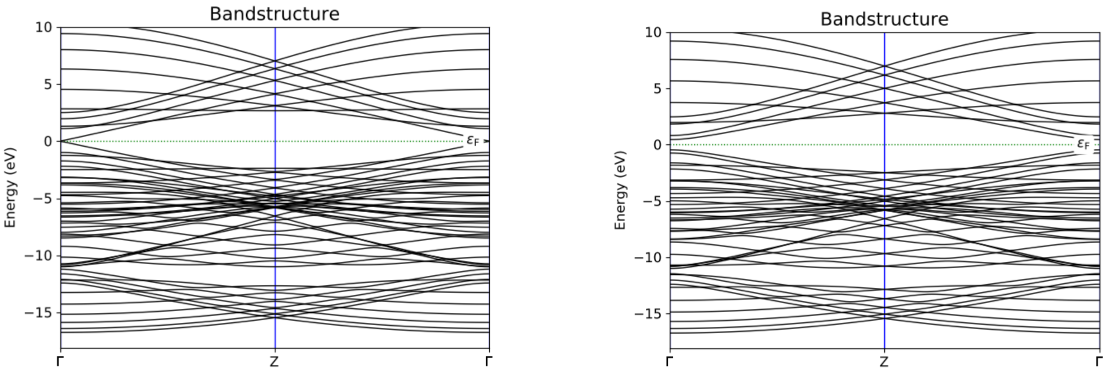

(a)

(b)

Figure 6.12: (a) Bandstructure for 11 and (b) 10 atom width acGNR nanoribbon configuration. Bands are plotted in terms of their energy vs the Brillouin zone route (i.e. Γ, Z as critical points in the route). Simulations carried out using Slater-Koster with Magsil1-1 parametrization

For this configuration, nanoribbons of 11 and 10 atoms of carbon wide were used as electrodes and channels, presenting a near-metallic behavior with a bandgap of $0.03eV$ and a semiconducting behavior with a bandgap of $0.9108eV$, respectively. The channel is also 6nm long as previous devices.

Although the electrodes of this device present more bandgap than the previous 17-atom wide electrodes, they present high conductance capability as well as depicts Figure 6.13. Also in this configuration the device in general presents low-temperature dependency in the red-shadowed zone (Figure 6.13a), except for $V_{GS} = 0.5V, -0.5V$. Taking into account that for gate voltages corresponding to $V_G > 0.5V$ & $VG < -0.5V$ we obtained the highest conductance values along with tunneling transport, we use these voltages later to analyze the sensing response of the device.

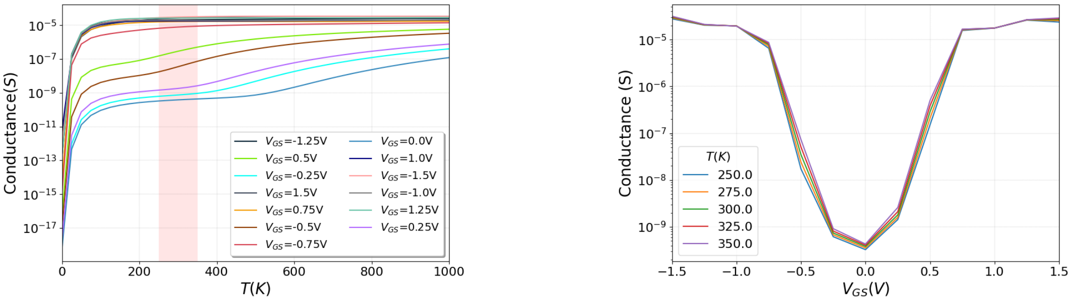

(A) (B)

Figure 6.13: (a) Conductance vs Temperature in electrodes and (b) Conductance vs gate voltage for 11-10-11 acGNR nanoribbon configuration

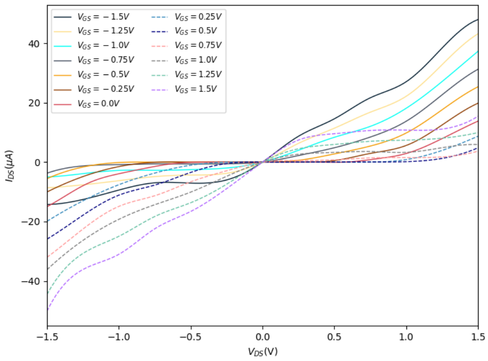

Figure 6.14: IV characteristics plot for configuration 11-10-11

Additionally for conductance, in Figure 6.13b shows its minimum value at $\sim V_{GS} = -0.2V$, meaning that the Fermi level is in the middle of the conduction and valence band at that voltage and that the conduction band is closer meaning electron dominant transport through the transistor (n-type).

Moreover, taking into account that we perform an in-silico analysis, we need a device geometry that offers a cost-effective solution. 17-10-17 device shows the best transport capabilities for example, at gate and drain-source voltages at $1.5V$ an output current of

$I_{DS} = 35 \upsilon A$c compared with $17 \upsilon A$ for 11-10-11. Therefore we chose this configuration to have the better transport at minimal geometry layout.

6.2.2 Pyrene Self Assembly Monolayer (SAM) IV Characteristics

We evaluate the IV characteristics of the transistor with and without the SAM layer on the channel. For this, we took the previously minimized geometry of the PBPBA on the nanoribbon and carried out transport calculations. The resulting Figure 6.15, confirms that the presence of pyrene ligands on the channel does not alter the transport properties of the bare transistor, especially for $-1.0V < V_{DS} < 1.0V$. This is a critical feature since it allows us to detect and distinguish the sensing signal of an amylose molecule bound to the PBPBA while the pyrene itself does not have a significant effect on the electronic response of the transistor.

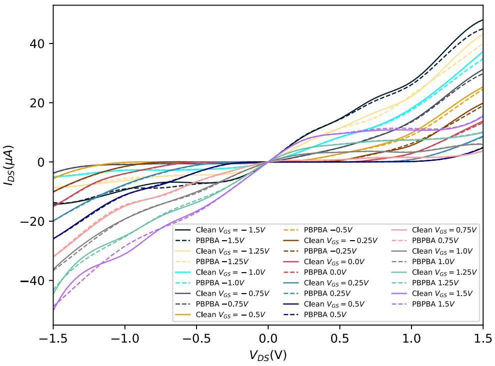

FIGURE 6.15: IV characteristics of 11-10-11 acGNR configuration comparing clean transistor and pyrenes on the channel (dotted lines)

6.2.3 IV characteristics with bound amyloses

After confirmation that the SAM layer will not affect considerably the detection of amylose through changes in the IV characteristics, we added linked amyloses to the SAM layer and analyzed how the analytes affect transport. Figure 6.16a depicts the IV characteristics of a device without a gate (a two-terminal device), the presence alone of the target molecules bound to the functionalized semiconducting junction does not alter the electronic transport in the device or at least is negligible.

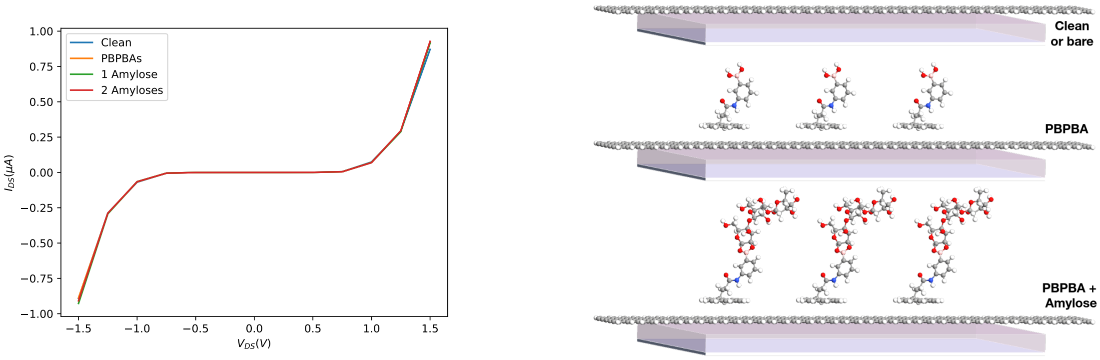

(A) (B)

FIGURE 6.16: (A) IV plot for the device 11-10-11 in two-terminal configuration (B) graphene three-terminal sensor with bare (top), functionalized with PBPBA (middle), and functionalized with bound amylose trimer molecules channel (bottom).

Therefore, for transport through the channel, we need a gate, then when we apply a gate voltage we could increase the density of states in the channel. We analyzed IV characteristics for different gate voltages, Figure 6.17, based on some that offer enough output current and where the SAM layer shows (in Figure 6.15) not to affect considerably the electronic response of the device.

We did perform IV characteristics varying the gate oxide of the device after realizing some design errors, we fixed it and also carried out simulations for a gate oxide in low-k and high-k dielectric (see Section A.2.1 in Appendix A). At high-k dielectrics in the gate oxide, we obtain better gate control over the channel, and therefore also more output current capabilities. Higher dielectric constant could be used to improve the device electronic response, we use silicon dioxide (i.e. $4.0\epsilon_0$ 3.58Å thick but it could be used Hafnium oxide or titanium dioxide same width (as Narendar et al. [51]) or also increase the thickness of gate oxide[1].

However, we present results here for silicon dioxide as the gate oxide, where we set different gate voltages and evaluate output or drain-source current as a function of the drain-source voltage for different content of amylose trimers bound to the PBPBA layer. We compare the bare (clean) semiconducting junction, the device functionalized with only 3PBPBAs and the device with 1, 2, or 3, amyloses bound. (Figure 6.16b)

We chose specifically gate voltages between $-1.0V < V_{GS} < 1.2V$, taking into account that at higher values of V_{DS} and V_{GS} convergence takes longer due to multiple factors:

---

[1] Taking into account that gate control is directly related to gate capacitance and this depends on gate oxide thickness or dielectric constant

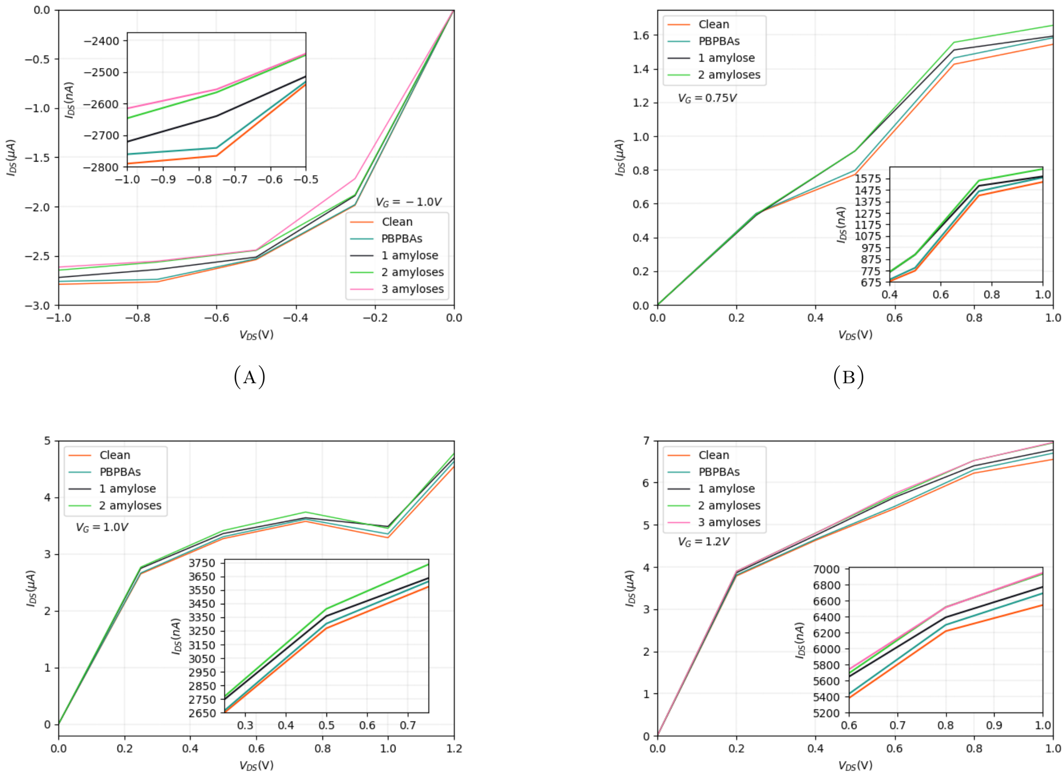

(A)

(B)

(C)

(D)

FIGURE 6.17: IV characteristics of 11-10-11 device for PBPBA SAM with no linked, one and two amylose molecules, and three for $V_{GS} = 1.2V$ compared to the clean reference performance (orange line). Inset depicts plot in nano amperes. (A) for a gate voltage of $-1.0V$, (B) for a gate voltage of $0.75V$ (C) for a gate voltage of $1.0V$ and (D) for a gate voltage of $1.2V$ and positive drain-source voltages

the number of atoms in the system increases with the presence of amyloses, higher voltages stress the system enough that tight binding approximations of the band structure no longer describes accurately the material making the self-consistent (SCF) difficult to reach convergence criteria. Besides, as Figure 6.15 portrays, for higher voltages, how the current plotline of the SAM layer starts to differ from the bare transistor.

Resulting IV characteristics of the device, after fixing V_{GS} at different values (Figure 6.17), show how linked amyloses have an effect on the transport through the channel. In Figure 6.17a for $V_{GS} = -1.0V$ we observe differences in output current of $50nA - 100nA$ for $V_{DS} = -1.0V$ to $-0.75V$ between the functionalized transistor with PBPBAs and 1 bound amylose; and a difference of $100nA$ between current response for 1 and 2 amyloses for the same range in V_{DS}. At a fixed gate voltage of $V_{GS} = 0.75, 1.0V$ there are differences in current between $50nA - 100nA$ as the respective inset plots of Figures 6.17b, 6.17c depict between the bare/functionalized transistor and 1, 2 or 3 amylose molecules. For gate voltage $1.2V$, inset in Figure 6.17d presents a difference range of $100-300nA$ for $V_{DS} = 0.6V$ to $1.0V$ between the functionalized transistor and 1 bound amylose, and $\sim 100nA - 150nA$ difference for the same range in V_{DS}.

Especially at voltages such as $V_G = -1.0V, 1.2V$ there is enough difference in the current signal to distinguish 1 from 2 amyloses. Amylose molecules that are bound to the pyrene SAM layer also present an electrostatic gating effect on the channel, (acting as a second gate) increasing the available density of states in the channel, however for 3 amyloses it appears that the device reaches saturation thus its current signal is hard to distinguish from the 2 amyloses signal. To wrap up, our device offers single amylose detection (for 1-2 molecules) bound to the SAM layer, and the working voltages would be $V_{GS} = 1.2V$ and $V_{DS} = 0.6V$ or $0.8V$.

6.2.4 Selectivity

PBPBA and the boronic acid at the reactive end, as we already mentioned, present an affinity to cis-diols which are characteristic of simple sugars molecules. This allows to detect amylose as it is conformed by glucose monomers, but we can not confirm the complete selectivity of the device because of the possible binding with other saccharides (i.e. sucrose, fructose) and polysaccharides (i.e. amylopectin) which also present cis-diols; this is an intrinsic drawback from our type of sensor that uses PBPBA.

	DFT	**ReaxFF**
Glucose	-12.1614 kcal/mol	-1.95317 kcal/mol

Table 6.3: Binding energies for glucose and PBPBAs in tetrahedral form. FHI-DZP [1] was used for DFT calculations and ReaxFF for molecular mechanics

We carried binding energies calculations with glucose, as this is the building block of amylose, still confirming binding with both methods using DFT and ReaxFF (even though accuracy was not the best and consistent compared with quantum mechanics results with DFT). In Table 6.3 results for a glucose monomer bound with the sp3-boronic acid form in the PBPBA are displayed along with amylose binding energies, here a difference of $6.35kcal/mol$ (in DFT) between amylose and glucose binding is observed, which although a small difference is not enough.

It is important to differentiate the response signal of the device when it detects amylose from other molecules. However, obtaining a selectivity and significant difference in the

IV characteristics or energy properties of the device is difficult to obtain only by the functionalization of the channel.

Further exploration needs to be done, to obtain high selectivity, for example, selectivity that uses the specific molecular conformation or geometry of the amylose could be designed (depending on the molecular form of amylose against other simple sugars or polysaccharides). In Section B.2 of Appendix B, we also present IV characteristics for a glucose monomer compared with an amylose trimer, where the electronic signature for 1 or 2 glucoses shows small differences in current.

On the other hand, it is also important to recognize that the sensor does provide selectivity from other chemical groups that might be present inside the cellular environment of plants i.e. hydroxyl, phenol, amino groups, etc, that correspond to other metabolites or molecules within the cell.

6.2.5 Device detection capabilities

By taking the transistor dimensions in Figure 4.6b, we estimate the Limit of Detection using the formula described in Section 5.3.5.1 (Chapter 5). Thus, we have an effective solvent volume of $2.33 \times 10^{-23} L$ (using the length of an extended 1PBPBA+ 1trimer-amylose complex physisorped on the GNR surface $\sim 3.5nm$, times the semiconducting junction's effective area $1.11nm \times 6.0nm = 6.66nm^2$) and Avogadro's number $N_A = 6.0221409 \times 10^{23} mol^{-1}$, and obtain an LOD of $7.1238/n \times 10^{-2} mol/L$ for an amylose trimer whose molecular weight is 642.4534 g/mol or $1.0668439 \times 10^{-21} g$; n corresponds to the number of nodes in nano-array and each node consisting of one acGNR FET transistor.

However, if we consider a footprint area, based on the total length and width of the FET as depicted in Figure 4.6b including edge passivation (namely $8.4nm \times 1.4nm = 11.76nm^2$) we estimate that a single node, would occupy actually no more than five times this area, (i.e. roughly $60nm^2$), taking into account interconnections between nodes, nano-fluidic channels to the channel, etc.

Furthermore, consider a sensing array of 1000×1000 nodes, this would have a LOD of 1 part per 2 million or $71.23 \mu M/L$ since our sensor can detect and measure single analytes (1 or 2 amyloses). Likewise, the upper detection and measurement of amyloses using such an array would be of 2 million amylose trimmers. If we use larger arrays, these would present an even lower LOD allowing higher sensitivity and detection capacity and the device would still perform at short-time exposures. Therefore, this design provides with a basic node architecture to conform more complex bio-sensing logic circuits that may be embedded in mobile devices to perform remote, real-time and high throughput detection of amylose trimers.

Chapter 7

Conclusions and future work

7.1 Conclusions

We demonstrated an in-silico Field-effect transistor (FET) design with electrodes (source, drain) and semiconducting channel junctions made out only by armchair graphene nanoribbons with a back-gate. For the final configuration we obtained a minimal footprint layout (11.76 nm^2) with high current capabilities, low dependency of temperature in conductivity.

We used a phenyl boronic acid molecule that selectively binds to diols chemical groups in amylose trimmers to functionalize a pyrene-based ligand (PBPBA) that also presents affinity to graphene, thus exhibiting strong physisorption capabilities to its surface. On that account, we obtained a general functionalization of the GNR, that does not perturb the intrinsic electronic response of the device and allowing any change in transport to be a direct effect of an amylose presence.

Additionally, we confirmed that the pyrene-moiety ligands remain absorbed on the graphene surface and bound to the amylose, even under physiological temperature conditions. Therefore providing physical, chemical and mechanical stabilization of the amylose trimer on the GNR, reducing its mobility and consequently noise in the electronic output signal.

By performing the electronic transport characterizations of the GNR channels, we determined that semi-empirical methods in quantum mechanics were the best approach to compute all calculations, specifically Slater Koster with magsil 1-1 parametrization[66] being the most cost-efficient compared with DFT FHI [1] and Hückel[67].

We also showed that the gate-oxide dielectric layer affects the gate control capabilities over the channel, resulting in higher current response capability of the device for high-k dielectrics (such as hafnium oxide, titanium dioxide, or other transition metal), albeit it did not affect single-analyte differentiation.

We achieved detection of single amylose-trimer molecules, for 1-2 molecules with differences in current between $100 - 300nA$ at relatively low voltages $V_G = 1.2V$ and $V_{DS} = 0.6 - 0.8V$, with a LOD of 7,123 $\times 10^{-2} mol/L$ for a single transistor. This provides the basic node for a potential 2D nano-array device architecture, e.g. 1000x1000 or $n \times n$ transistors with LOD of 71.23 $\mu M/L$ or 7,123/n $\times 10^{-2} mol/L$ respectively (assuming a node footprint of $11.76nm^2$ and a volumetric height of $3.5nm$, for a total of $41.26nm^3$ per detection node).

Finally, as a general and more personal observation, during this project not only I strengthened and applied concepts learned during my electrical engineering coursework, but I learned advanced concepts and acquired basic knowledge of quantum transport and computational methods useful to model nano-electronic devices; also applying all of this in an interdisciplinary field like bio-sensing devices which involved to understand other biology and chemistry concepts too. During this project, I also gained basic research and analytical skills, which would be very useful if I decide to continue with my graduate studies in related fields, whether I decide for academia or industry as career paths.

7.2 Future work

A more exhaustive exploration and analysis between different boronic acids can be done to find the right variation, that allows the Sp^3 form at lower pH values being more compatible at physiological conditions.

Further electronic calculations can be performed comparing the response of the device to other amylose polymers at different sizes, evaluate how that affects the device response and whether the amylose monomer content could be differentiated via their electronic signature. Getting to know the amylose content in crops is of major interest since amylose content provides nutritional information about the product.

We proposed PBPBA as a ligand, it has an affinity to cis-diols and these are present in other simple sugars apart from amylose and glucose. Therefore, additional exploration and study of the device response to other polysaccarides and other forms to achieve specific selectivity of amylose needs to be done.

Another type of multi-terminal device which does not need semiconducting graphene could be evaluated such as Hall-bars or a crossbar nanomesh using graphene nanoribbons or carbon nanotubes, using the same type of functionalization with pyrene moieties with specific affinity to amylose could be used to stabilize and detect the analyte.

Finally, we need further studies to generalize the behaviour of our device, to evaluate its fabrication and to confirm sensing capabilities experimentally. Maybe not using GNRFET as designed and proposed here, because of such precise fabrication is difficult to achieve, but explore commercially available graphene devices and use the same sensing method to measure starch or amylose.

Bibliography

[1] Volker Blum, Ralf Gehrke, Felix Hanke, Paula Havu, Ville Havu, Xinguo Ren, Karsten Reuter, and Matthias Scheffler. Ab initio molecular simulations with numeric atom-centered orbitals. *Computer Physics Communications*, 180(11):2175–2196, 2009.

[2] Diane M Beckles. Use of biotechnology to engineer starch in cereals. *Encyclopedia of Biotechnology in Agriculture and Food*, 2014.

[3] Ming-Kwei Lee Simon M. Sze. *Semiconductor Devices: Physics and Technology*, chapter 1, pages 23–29. Wiley, 3 edition, 2012.

[4] Jamie H Warner, Franziska Schaffel, Mark Rummeli, and Alicja Bachmatiuk. *Graphene: Fundamentals and emergent applications*, chapter 6.1, pages 333–346. Newnes, 2012.

[5] Juan M. Marmolejo-Tejada and Jaime Velasco-Medina. Review on graphene nanoribbon devices for logic applications. *Microelectronics Journal*, 48:18 – 38, 2016.

[6] Cheng Wang, Jinho Kim, Yibo Zhu, Jaeyoung Yang, Gwan-Hyoung Lee, Sunwoo Lee, Jaeeun Yu, Renjun Pei, Guohua Liu, Colin Nuckolls, et al. An aptameric graphene nanosensor for label-free detection of small-molecule biomarkers. *Biosensors and Bioelectronics*, 71:222–229, 2015.

[7] Supriyo Datta. Nanoscale device modeling: the green's function method. *Superlattices and Microstructures*, 28(4):253 – 278, 2000.

[8] Andres Jaramillo-Botero, Jamil Tahir-Kheli, Paul von Allmen, and William A Goddard III. Multiscale, multiparadigm modeling for nanosystems characterization and

design. In *Handbook of Nanoscience, Engineering, and Technology*, pages 958–1005. CRC Press, 2018.

[9] Andrés Jaramillo-Botero. Computational nanoscale science and engineering. University Lecture, 2020.

[10] Brighid Pappin, Milton J Kiefel, and Todd A Houston. Boron-carbohydrate interactions. *Carbohydrates-comprehensive studies on glycobiology and glycotechnology*, 2012.

[11] Chaker Tlili, Sushmee Badhulika, Thien-Toan Tran, Ilkeun Lee, and Ashok Mulchandani. Affinity chemiresistor sensor for sugars. *Talanta*, 128:473–479, 2014.

[12] Andres Jaramillo-Botero and Juan M Marmolejo-Tejada. All-armchair graphene nanoribbon field-effect uridine diphosphate glucose sensor: First-principles in-silico design and characterization. *IEEE Sensors Journal*, 19(11):3975–3983, 2019.

[13] Robert T Furbank and Mark Tester. Phenomics–technologies to relieve the phenotyping bottleneck. *Trends in plant science*, 16(12):635–644, 2011.

[14] Luis M Solarte, Ruben D Escandon, Diana Hermith, Pedro M Hernandez-Acosta, Eugenio Tamura, Luis E Tobon, Hernan D Benitez-Restrepo, and Andres Jaramillo-Botero. Phenosense midterm report. Technical report, Pontificia Universidad Javeriana Cali and California Institute of Technology and International Center for Tropical Agriculture (CIAT), February 2017.

[15] RB Smith, EC Lougheed, EW Franklin, and I McMillan. The starch iodine test for determining stage of maturation in apples. *Canadian Journal of Plant Science*, 59(3):725–735, 1979.

[16] Alison M Smith and Samuel C Zeeman. Quantification of starch in plant tissues. *Nature protocols*, 1(3):1342–1345, 2006.

[17] Barbara Pfister and Samuel C Zeeman. Formation of starch in plant cells. *Cellular and Molecular Life Sciences*, 73(14):2781–2807, 2016.

[18] S.P. Mohanty. Biosensors : A Tutorial Review Biosensors : A Tutorial Review. *IEEE Potentials*, 25(APRIL 2006):35–40, 2015.

[19] David Seung. Amylose in starch: Towards an understanding of biosynthesis, structure and function. *New Phytologist*, 228(5):1490–1504, 2020.

[20] B.G. Streetman and S. Banerjee. *Solid State Electronic Devices*, chapter 3.1, pages 61–71. Prentice Hall series in solid state physical electronics. Prentice Hall, 2000.

[21] Bryan W. Boudouris. Organic electronic devices. unit 2: Electronic structure. ONLINE. `https://nanohub.org/courses/oed`, 2015.

[22] Sima Dimitrijev. *Principles of semiconductor devices*, chapter 8, pages 5–10. Oxford university press, 2012.

[23] Jamie H Warner, Franziska Schaffel, Mark Rummeli, and Alicja Bachmatiuk. *Graphene: Fundamentals and emergent applications*, chapter 2.1, pages 296–349. Newnes, 2012.

[24] Elnaz Akbari, Vijay K Arora, Aria Enzevaee, Mohamad T Ahmadi, Mehdi Saeidmanesh, Mohsen Khaledian, Hediyeh Karimi, and Rubiyah Yusof. An analytical approach to evaluate the performance of graphene and carbon nanotubes for nh3 gas sensor applications. *Beilstein journal of nanotechnology*, 5(1):726–734, 2014.

[25] Jamie H Warner, Franziska Schaffel, Mark Rummeli, and Alicja Bachmatiuk. *Graphene: Fundamentals and emergent applications*, chapter 2.5, pages 33–49. Newnes, 2012.

[26] Li Yang, Cheol-Hwan Park, Young-Woo Son, Marvin L Cohen, and Steven G Louie. Quasiparticle energies and band gaps in graphene nanoribbons. *Physical Review Letters*, 99(18):186801, 2007.

[27] Michiko Kusunoki, Wataru Norimatsu, Jianfeng Bao, Koichi Morita, and Ulrich Starke. Growth and features of epitaxial graphene on sic. *Journal of the Physical Society of Japan*, 84(12):121014, 2015.

[28] Gholam Reza Yazdi, Tihomir Iakimov, and Rositsa Yakimova. Epitaxial graphene on sic: A review of growth and characterization. *Crystals*, 6(5):53, 2016.

[29] Wataru Norimatsu and Michiko Kusunoki. Epitaxial graphene on sic {0001}: advances and perspectives. *Physical Chemistry Chemical Physics*, 16(8):3501–3511, 2014.

[30] Deana Kwong Hong Tsang. *Chemically functionalised graphene biosensor for the label-free sensing of exosomes.* PhD thesis, Imperial College London, 2019.

[31] Ernie W Hill, Aravind Vijayaragahvan, and Kostya Novoselov. Graphene sensors. *IEEE Sensors Journal*, 11(12):3161–3170, 2011.

[32] Nathaniel S Green and Michael L Norton. Interactions of dna with graphene and sensing applications of graphene field-effect transistor devices: A review. *Analytica chimica acta*, 853:127–142, 2015.

[33] Giwan Seo, Geonhee Lee, Mi Jeong Kim, Seung-Hwa Baek, Minsuk Choi, Keun Bon Ku, Chang-Seop Lee, Sangmi Jun, Daeui Park, Hong Gi Kim, et al. Rapid detection of covid-19 causative virus (sars-cov-2) in human nasopharyngeal swab specimens using field-effect transistor-based biosensor. *ACS nano*, 14(4):5135–5142, 2020.

[34] Supriyo Datta. *Lessons from Nanoelectronics:A New Perspective on Transport - Part B*, chapter Contact-ing Schroedinger, pages 19–38. World Scientific, 2nd edition, 2018.

[35] Max Born and Robert Oppenheimer. Zur quantentheorie der molekeln. *Annalen der physik*, 389(20):457–484, 1927.

[36] Luis EF Foa Torres, Stephan Roche, and Jean-Christophe Charlier. *Introduction to graphene-based nanomaterials: from electronic structure to quantum transport*, chapter Appendix A.Electronic Structure Calculations: The Density Functional Theory, pages 354–372. Cambridge University Press, 2020.

[37] Llewellyn H Thomas. The calculation of atomic fields. In *Mathematical proceedings of the Cambridge philosophical society*, volume 23, pages 542–548. Cambridge University Press, 1927.

[38] E Fermi. On quantizing an ideal monatomic gas. *Rend. Lincei*, 145:1–9, 1926.

[39] Paul AM Dirac. Note on exchange phenomena in the thomas atom. In *Mathematical proceedings of the Cambridge philosophical society*, volume 26, pages 376–385. Cambridge University Press, 1930.

[40] Pierre Hohenberg and Walter Kohn. Inhomogeneous electron gas. *Physical review*, 136(3B):B864, 1964.

[41] Walter Kohn and Lu Jeu Sham. Self-consistent equations including exchange and correlation effects. *Physical review*, 140(4A):A1133, 1965.

[42] Supriyo Datta. *Lessons from Nanoelectronics: A New Perspective on Transport - Part B*, chapter NEGF Method, pages 43–74. World Scientific, 2nd edition, 2018.

[43] Supriyo Datta. *Lessons from Nanoelectronics: A New Perspective on Transport - Part A*, chapter Quasi-Fermi Levels, pages 121–138. World Scientific, 2nd edition, 2017.

[44] Dong C Liu and Jorge Nocedal. On the limited memory bfgs method for large scale optimization. *Mathematical programming*, 45(1):503–528, 1989.

[45] Kyoung Taek Kim, Jeroen JLM Cornelissen, Roeland JM Nolte, and Jan CM van Hest. Polymeric monosaccharide receptors responsive at neutral ph. *Journal of the American Chemical Society*, 131(39):13908–13909, 2009.

[46] Jun Yan, Greg Springsteen, Susan Deeter, and Binghe Wang. The relationship among pka, ph, and binding constants in the interactions between boronic acids and diols—it is not as simple as it appears. *Tetrahedron*, 60(49):11205–11209, 2004.

[47] William LA Brooks, Christopher C Deng, and Brent S Sumerlin. Structure–reactivity relationships in boronic acid–diol complexation. *ACS omega*, 3(12):17863–17870, 2018.

[48] Jamie H Warner, Franziska Schaffel, Mark Rummeli, and Alicja Bachmatiuk. *Graphene: Fundamentals and emergent applications*. Newnes, 2012.

[49] Vasilios Georgakilas, Michal Otyepka, Athanasios B Bourlinos, Vimlesh Chandra, Namdong Kim, K Christian Kemp, Pavel Hobza, Radek Zboril, and Kwang S Kim. Functionalization of graphene: covalent and non-covalent approaches, derivatives and applications. *Chemical reviews*, 112(11):6156–6214, 2012.

[50] Carrie Haslam, Samar Damiati, Toby Whitley, Paul Davey, Emmanuel Ifeachor, and Shakil A Awan. Label-free sensors based on graphene field-effect transistors for the detection of human chorionic gonadotropin cancer risk biomarker. *Diagnostics*, 8(1):5, 2018.

[51] Vadthiya Narendar, SK Gupta, and Shikhar Saxena. First principle study of doped graphene for fet applications. *Silicon*, 11(1):277–286, 2019.

[52] Malkolm Hinnemo, Jie Zhao, Patrik Ahlberg, Carl Hägglund, Viktor Djurberg, Ralph H Scheicher, Shi-Li Zhang, and Zhi-Bin Zhang. On monolayer formation of pyrenebutyric acid on graphene. *Langmuir*, 33(15):3588–3593, 2017.

[53] Steve Plimpton. Fast parallel algorithms for short-range molecular dynamics. *Journal of computational physics*, 117(1):1–19, 1995.

[54] C C W Verlackt, E C Neyts, T Jacob, D Fantauzzi, M Golkaram, Y-K Shin, A C T van Duin, and A Bogaerts. Atomic-scale insight into the interactions between hydroxyl radicals and DNA in solution using the ReaxFF reactive force field. *New Journal of Physics*, 17(10):103005, oct 2015.

[55] H. M. Aktulga, J. C. Fogarty, S. A. Pandit, and A. Y. Grama. Parallel reactive molecular dynamics: Numerical methods and algorithmic techniques. *Parallel Computing*, 38:245–259, 2012.

[56] Leandro Martínez, Ricardo Andrade, Ernesto G Birgin, and José Mario Martínez. Packmol: a package for building initial configurations for molecular dynamics simulations. *Journal of computational chemistry*, 30(13):2157–2164, 2009.

[57] Wataru Shinoda, Motoyuki Shiga, and Masuhiro Mikami. Rapid estimation of elastic constants by molecular dynamics simulation under constant stress. *Physical Review B*, 69(13):134103, 2004.

[58] Søren Smidstrup, Daniele Stradi, Jess Wellendorff, Petr A Khomyakov, Ulrik G Vej-Hansen, Maeng-Eun Lee, Tushar Ghosh, Elvar Jónsson, Hannes Jónsson, and Kurt Stokbro. First-principles green's-function method for surface calculations: A pseudopotential localized basis set approach. *Physical Review B*, 96(19):195309, 2017.

[59] Søren Smidstrup, Troels Markussen, Pieter Vancraeyveld, Jess Wellendorff, Julian Schneider, Tue Gunst, Brecht Verstichel, Daniele Stradi, Petr A Khomyakov, Ulrik G Vej-Hansen, et al. Quantumatk: An integrated platform of electronic and atomic-scale modelling tools. *J. Phys: Condens. Matter*, 32:015901, 2020.

[60] 2020. QuantumATK version Q-2020.09, Synopsys QuantumATK (www.synopsys.com/silicon/quantumatk.html).

[61] John P Perdew, Kieron Burke, and Matthias Ernzerhof. Generalized gradient approximation made simple. *Physical review letters*, 77(18):3865, 1996.

[62] Stefan Grimme, Jens Antony, Stephan Ehrlich, and Helge Krieg. A consistent and accurate ab initio parametrization of density functional dispersion correction (dft-d) for the 94 elements h-pu. *The Journal of chemical physics*, 132(15):154104, 2010.

[63] Marcus Elstner, Dirk Porezag, G Jungnickel, J Elsner, M Haugk, Th Frauenheim, Sandor Suhai, and Gotthard Seifert. Self-consistent-charge density-functional tight-binding method for simulations of complex materials properties. *Physical Review B*, 58(11):7260, 1998.

[64] Mads Brandbyge, José-Luis Mozos, Pablo Ordejón, Jeremy Taylor, and Kurt Stokbro. Density-functional method for nonequilibrium electron transport. *Physical Review B*, 65(16):165401, 2002.

[65] Thomas D Kühne, Marcella Iannuzzi, Mauro Del Ben, Vladimir V Rybkin, Patrick Seewald, Frederick Stein, Teodoro Laino, Rustam Z Khaliullin, Ole Schütt, Florian Schiffmann, et al. Cp2k: An electronic structure and molecular dynamics software package-quickstep: Efficient and accurate electronic structure calculations. *The Journal of Chemical Physics*, 152(19):194103, 2020.

[66] J Frenzel, AF Oliveira, N Jardillier, T Heine, and G Seifert. Semi-relativistic, self-consistent charge slater-koster tables for density-functional based tight-binding (dftb) for materials science simulations. *Zeolites*, 2(3):7, 2004.

[67] Kurt Stokbro, Dan Erik Petersen, Søren Smidstrup, Anders Blom, Mads Ipsen, and Kristen Kaasbjerg. Semiempirical model for nanoscale device simulations. *Physical Review B*, 82(7):075420, 2010.

[68] Péter Pulay. Convergence acceleration of iterative sequences. the case of scf iteration. *Chemical Physics Letters*, 73(2):393–398, 1980.

Appendix A

Additional simulations

A.1 Computational methods comparison

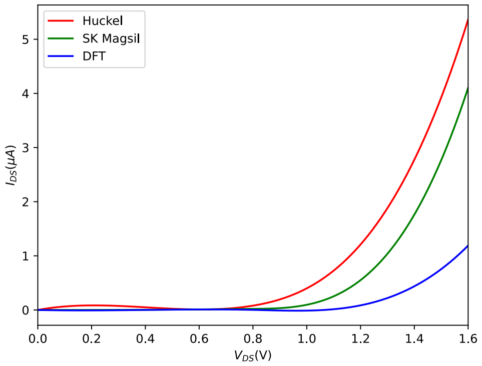

FIGURE A.1: Comparison of IV curve for 11-10-11 acGNR configuration device at $V_G = 0.5V$, using Semi-empirical methods (Slater Koster with Magsil parametrization and Extended Hückel with Hoffmann parameters) and Density Functional Theory-based FHI-DZP

We performed transport calculations mostly with semi-empirical approximations using DFTB. We started in configuration 14-7-14 with Slater Koster with CP2K parameter integration. However for 11-7-11, 11-10-11, 17-10-17 acGNRFET configurations, we changed the parameter set since CP2K does not support Boron atoms and at this point, we needed those parameters for the Boron atom present in the chosen pyrene moiety PBPBA. Therefore, IV characterization was from there on, carried with DFTB, Slater Koster basis set along the general-purpose parameter set Magsil-1-1 [66] (which works for hydrogen, boron, carbon, nitrogen, and oxygen atoms present in our device). We also carried some simulations for 11-7-11 and 11-10-11 using Extended Hückel [67] with Hoffmann basis sets. Although the latter method covered parametrization for Boron atoms, the convergence of the self-consistent and signal response stabilization occurred using more than 151 k-points (as Figure A.2 shows), making the simulations more expensive than using 101 kpoints with Slaker Koster. Besides, Slater Koster results showed closer values when compared with DFT, contrary to Hückel as Figure A.1 shows. DFT becomes an expensive method for systems of atoms >1000, compared to DFTB, therefore it was not an option for our limited resources.

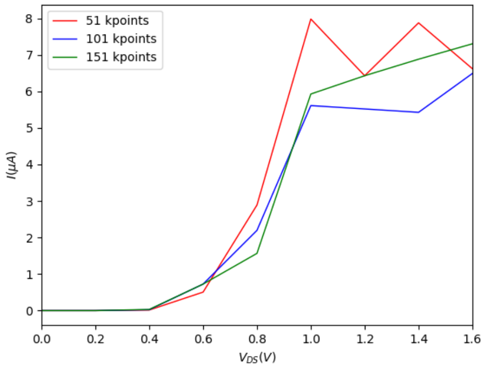

Figure A.2: Comparison of IV curves for 11-7-11 acGNR configuration device at $V_G = 1.5V$, using Semi-empirical method (Extended Hückel with Hoffmann parameters) for different k-points samplings along the C direction.

A.2 11-10-11 additional calculations

In this section, we present additional results for configuration 11-10-11.

A.2.1 Gate-dielectric calculations

The dielectric layer used to separate gate metallic contact from the channel in a FET device should work as an insulator between channel and gate, with high capacitance capabilities. Higher oxide capacitance C_{ox} means higher gate control over the channel, where the relationship with the material of gate oxide is described by:

$$C_{ox} = \frac{\epsilon_r \epsilon_0}{t_{ox}} \tag{A.1}$$

where ϵ_r is the relative permittivity of the material used as gate oxide (normally silicon oxide) and ϵ_0 the permittivity of vacuum, and the thickness of the oxide t_{ox}. At higher values of ϵ_r or small values of thickness, higher oxide capacitance, however, very small thickness is not desired because dielectric breakdown occurs and leakage currents by quantum tunneling.

We present following, some calculations of I-V characteristics we computed, where we show the effects of gate dielectric permittivities on the electronic transport of the device.

A.2.1.1 Vacuum between gate dielectric and graphene

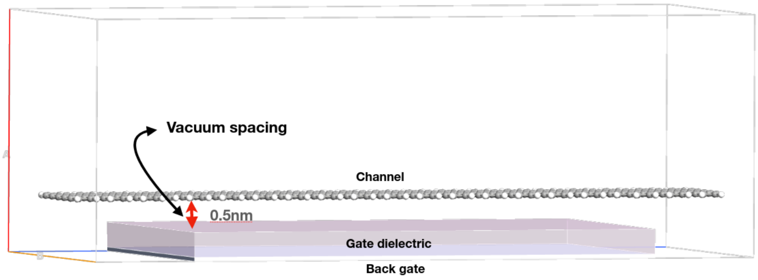

FIGURE A.3: 11-10-11 device with $5A$ vacuum between the gate oxide and channel

The results that we obtained and showed until now, correspond to the device geometry described previously, where the GNR channel has direct contact with the gate oxide. However, we also carried out simulations where accidentally the GNR channel had a vacuum distance of five angstroms from the gate oxide. This detail in the device architecture affects considerably the electronic response of the device since the gate oxide is critical for the modulation of current through the channel. With such a gap of vacuum present between both layers, the real gate oxide dielectric constant changes, and it no longer is described by $\epsilon_r = 4.0$ of the Silicon Oxide alone but lower, since $\epsilon_r 0 = 1.0$ and we have both permittivities. We performed electronic transport calculations for this configuration as we show in Figure A.4. The most notable change in the device IV characteristics is how the output current capabilities of the transistor are affected, showing for example for $V_{GS} = 1.0V$an $I_{DS} \sim -20\mu A$, when at the corrected device (in Figure 6.15) the output current is higher being $I_{DS} = 30\mu A$.

Figure A.4a shows how the pyrene SAM layer still does not affect in a significant way transport compared with the clean transistor. This means that if we change the gate dielectric of the device, we could still expect the sensor to detect amylose through the

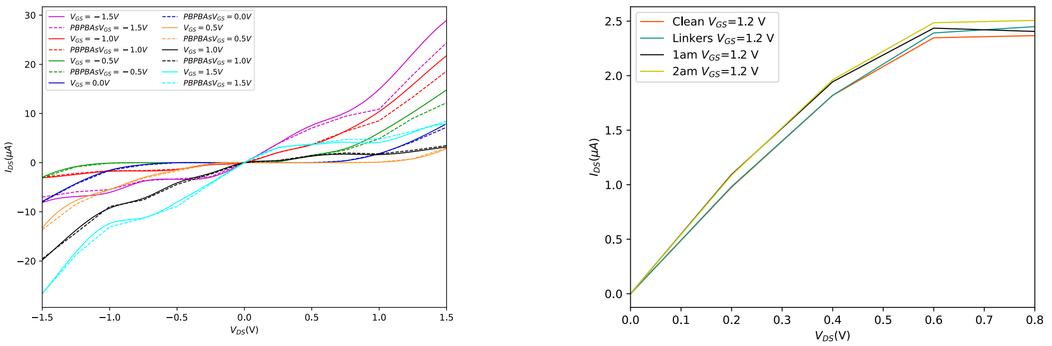

(A) (B)

Figure A.4: (A) IV characteristics plot for 11-10-11 acGNR configuration for clean transistor compared with PBPBA SAM with no linked molecules (dotted lines) (B)Comparison for PBPBA SAM with no linked, one and two amylose molecules, compared to the clean reference performance (orange line)

shift in current it induces through the channel without worrying that the SAM layer might interfere in those measurements. This is confirmed in6.12b, where through an output current difference in nano amperes we could still detect amylose. However, having this vacuum layer is not optimal because the vacuum does not isolate, thus it could result in leakage currents by tunneling from the gate.

A.2.1.2 Gate-dielectric permittivity

Changes in the response of the transistor due to the vacuum present between the graphene nanoribbon channel and the gate oxide, raise the question of how the dielectric constant of the gate oxide may affect the detection of amylose analytes. For this reason, we also evaluated the same device of Figure 6.17, but changing the dielectric relative permittivity from previous $\epsilon_r = 4.0$ to a much lower and higher value (high-k dielectric), $\epsilon_r = 2.0$ and $\epsilon_r = 100$ respectively.

As we noticed previously with the vacuum layer, at lower dielectric constants (i.e. $\epsilon_r = 2.0$ in Figure A.5a) I_{DS} decreases, and the opposite effect happens at high-k (Figure A.5b) when we notice how current increases. However, the difference in I_{DS} between the bare/functionalized device with one, two, or three amyloses bound remains almost the same $50 - 200nA$, being that at high-k dielectrics we change the device output current capabilities and a more consistent differentiation between 1 and 2 amyloses.

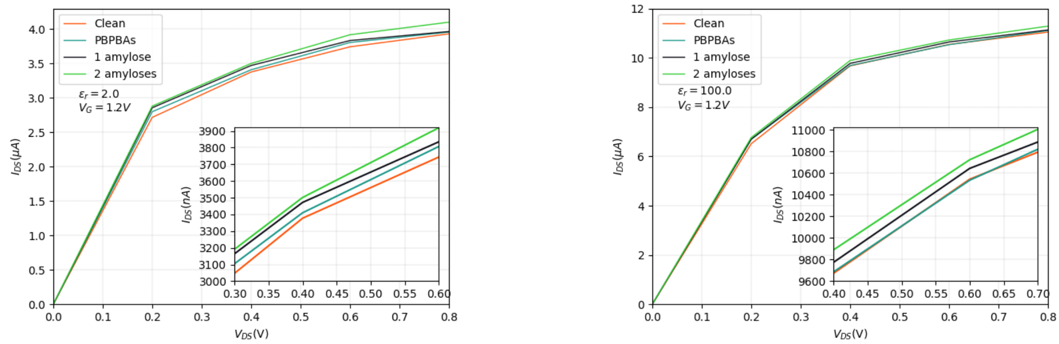

(A) (B)

FIGURE A.5: IV characteristics of 11-10-11 acGNRFET with (A) low gate dielectric constant $\epsilon_r = 2.0$ (B) high gate dielectric constant $\epsilon_r = 100$. Comparison for PBPBA SAM with no linked, one and two amylose molecules, compared to the clean reference performance (orange line)

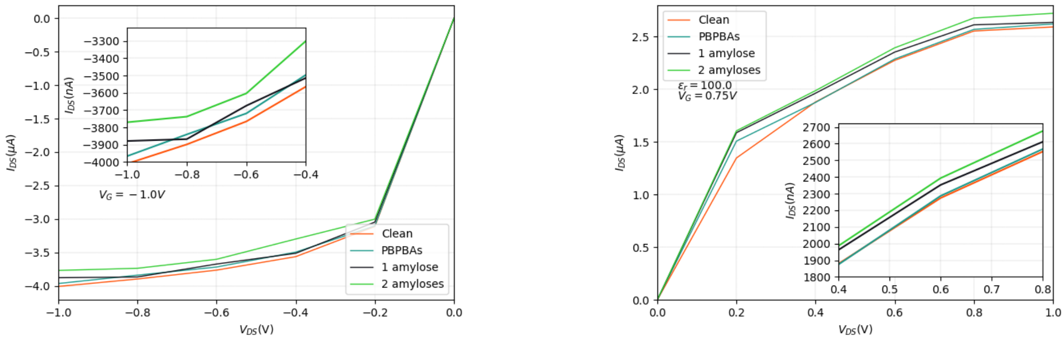

(A) (B)

FIGURE A.6: IV characteristics of 11-10-11 acGNRFET with high gate dielectric constant $\epsilon_r = 100$. Comparison for PBPBA SAM with no linked, one and two amylose molecules, compared to the clean reference performance (orange line) for (A) $V_{GS} = -1.0V$ and (B) $V_{GS} = 0.75V$

Nevertheless, if we want to improve the output current capability of the device, high-k dielectrics could be used (hafnium oxide, titanium oxide, or other transition metals) such as Narendar et. al [51] use in a first-principles study of gnrFETs also performed in QuantumATK.

Also as the gate oxide effect on the channel also depends on the thickness of this layer (by the oxide capacitance), further simulations could be performed too.

A.2.2 With Extended Hückel, IV characteristics

Results for simulations in the configuration of 11-10-11 with a vacuum layer (of 5 Å between the graphene channel and gate oxide. Maximum output current is higher but also because Hückel is not as accurate as SK-Magsil when compared with DFT as depicted before in FigureA.1.

DFTB type	**AC-GNR 11**	**AC-GNR 10**
Huckel	0.057607 eV	1.096824 eV
SK-magsil	0.0321664 eV	0.915891 eV

TABLE A.1: Bandgaps of AC-GNR for device 11-10-11 with DFTB Extended Hückel and Slater-Koster magsil DFTB parameters

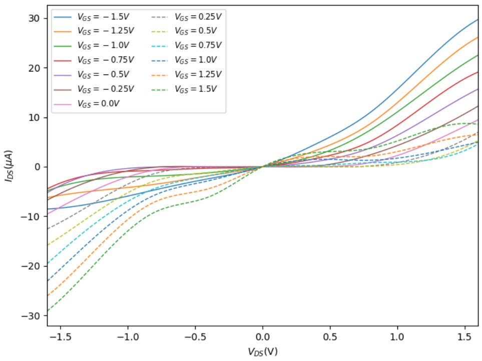

FIGURE A.7: IV characteristics plot for configuration 11-10-11 with 5Avaccuum between the gate oxide and channel

Similar behavior of the pyrene SAM layer is observed as with SK-Magsil results, it especially affects electronic properties of the channel for higher negative V_{GS} and higher values of V_{DS}.

A.2.3 11-10-11 with DFT, Double Zeta Polarized

Some IV characteristics for 11-10-11 configuration were carried using DFT with GGA exchange-correlation, Perdew-Burkey-Ernzenhof (PBE), and FHI pseudopotentials with DZP basis sets. Negative V_{DS} voltages at $V_G = 1.0V$ exhibit high values of output current that, we thought, would lead to a higher difference in current between 1 and 2 amyloses. However, when using DFTB with Slater Koster we had convergence problems and decided to use DFT, for its accuracy. The consistent difference in current for 1

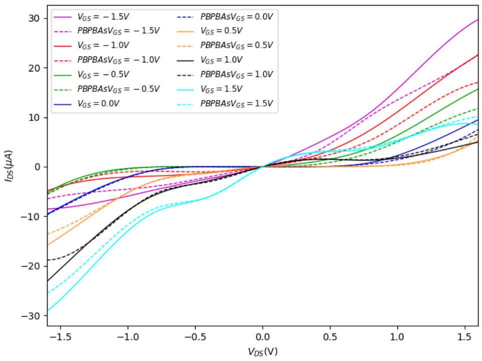

Figure A.8: IV characteristics plot for configuration 11-10-11 with 5Å vaccuum between the gate oxide and channel and PBPBA SAM on the channel using Extended Hückel

and 2 amyloses was not achieved, making it hard to distinguish amyloses from the clean transistor as Figure A.9 shows:

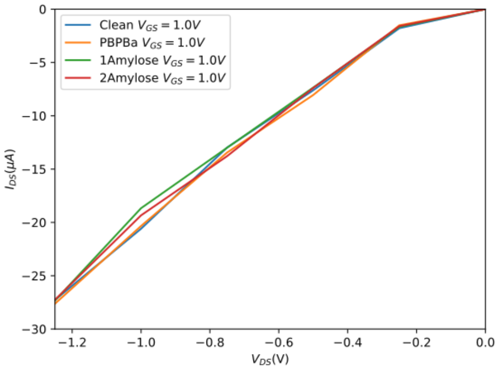

Figure A.9: IV characteristics plot for configuration 11-10-11 with PBPBA SAM (dotted lines) on the channel using DFT with FHI-Double Zeta Polarized[1]

This was one of the reasons we decided for positive values of V_{DS} at positive values of V_G and negative values of V_{DS} at positive V_G where we obtained amylose detection and differentiation with DFTB (shown in Chapter 6. However, we did not perform positive values of V_{DS} for Figure A.9 simulations with DFT because of its high computational cost compared with DFTB. In Smidstrup et al. [59] they compare DFT and DFTB performance as implemented in QuantumATK.

Appendix B

Simulations with other molecules

B.1 ADP-Glucose

B.1.1 Binding energies

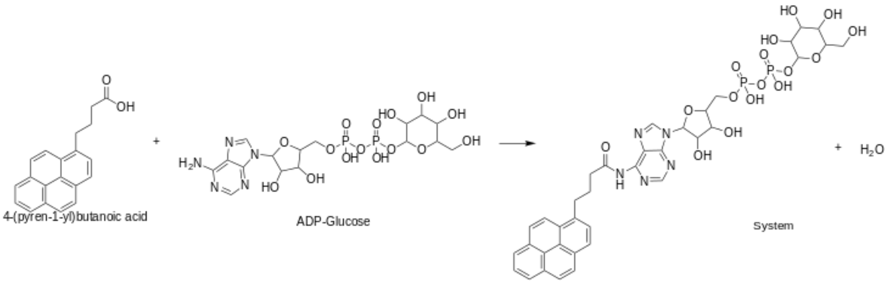

FIGURE B.1: ADP Glucose and Pyrene Butyric Acid reaction schematic diagram

The reaction between the pyrene butyric acid (PBA) and the ADP-Glucose, happens between the carboxylic group in the former end the amino group in the latter forming a peptide bond. We performed binding energy calculations using DFT and a REAXFF from Verlackt et. al [54].

	DFT(FHI-DZP)	**REAXFF**
E_{bind}	-15.473 kcal/mol	-34.525 kcal/mol

TABLE B.1: Binding energies for ADP-Glucose molecule and Pyrene butyric acid (PBA)

This reaction presents binding energy as shown in Table B.1. ReaxFF and DFT methods show a difference of 10kcal/mol. However, in Jaramillo et. al [12] the same force field was used and showed differences within the same range ($10kcal/mol$) for binding energies. ADP-glucose could be used as well to detect indirectly starch.

B.1.2 Transport properties

Since the device for detection of ADP-Glucose does not present Boron atoms, only H, C, N, O, and phosphorus (P) atoms, we took the chance to compare two different Slater Koster methods (CP2K) and the one we used for the analysis of the 11-10-11 device Slater Koster with Magsil 1-1 parameters. 17-10-17 device was used, with a 6nm channel long.

Figure B.2a shows a clear difference between the presence of 1 and 2 ADPs bound to the PBA. However, B.2b shows little difference between the presence of 1 and 2 ADPs, maybe because the DFTB parametrization of SK Magsil is optimized for atomic systems with boron.

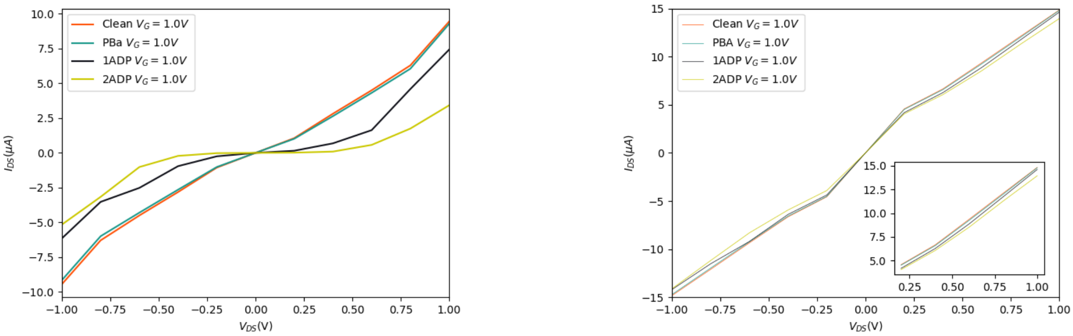

(A) (B)

FIGURE B.2: (A) The IV-Characteristics for 17-10-17 configuration using CP2K Slater Koster. (B) The IV-Characteristics for 17-10-17 configuration using Magsil 1-1 Slater Koster

B.2 Glucose

B.2.1 IV-Characteristics

Furthermore, as glucose is the building block for other sugars too (sucrose, amylopectin) we performed IV characteristics with one, two, and three glucoses bound to the pyrene SAM layer on the channel and compared it with one amylose response as Figure B.3

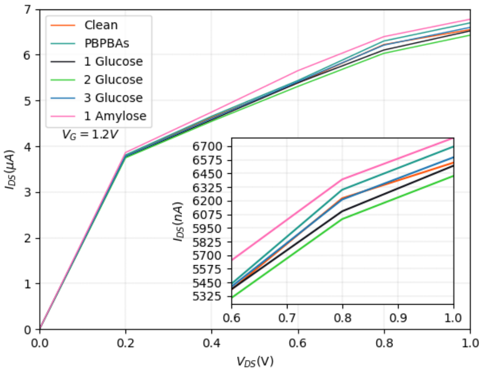

Figure B.3: IV characteristics of 11-10-11 device for PBPBA SAM with no linked, one, two, and three glucose molecules, compared to the clean reference performance (orange line); and the IV response for PBPBA linked to one amylose molecule

shows. Differences in the output current of $\sim 100nA$ between clean transistor, and 1 glucose, and between 1 and 2 glucose molecules bound to the SAM layer; additionally a difference of $250nA - 350nA$ for V_{GS} =between 1 amylose 1 or 2 glucose in the output current. Glucose molecules on the electronic device response show the opposite effect compared with amylose, resulting in lower output current; however, the 3 glucoses bound show a similar electronic response as the clean transistor, being problematic. Further exploration to guarantee selectivity and differentiation of amylose detection against other monosaccharides or polysaccharides must be done.